APOE3-R136S mutation confers resilience against tau pathology via cGAS-STING-IFN inhibition

Sarah Naguib[1,4], Eileen Ruth Torres[1,4], Chloe Lopez-Lee[1,2,4], Li Fan[1], Maitreyee Bhagwat[1], Kendra Norman[1], Se-In Lee[1], Jingjie Zhu[1], Pearly Ye[1], Man Ying Wong[1], Tark Patel[3], Sue-Ann Mok[3], Wenjie Luo[1], Subhash Sinha[1], Mingrui Zhao[1], Shiaoching Gong[1], and Li Gan[1,2*]

[1] Helen and Robert Appel Institute for Alzheimer's Disease Research, Brain and Mind Research Institute, Weill Cornell Medicine, New York, NY

[2] Neuroscience Graduate Program, Weill Cornell Medicine, New York, NY

[3] Department of Biochemistry, University of Alberta, Edmonton, AB T6G 2H7, Canada

[4] Authors contributed equally

[*]Correspondence: lig2033@med.cornell.edu

One-sentence summary:

The R136S mutation on APOE3 enhances resistance to tau-related disease processes by downregulating the cGAS-STING-IFN signaling pathway.

Summary

The Christchurch mutation (R136S) on the *APOE3* (*E3*$^{S/S}$) gene is associated with low tau pathology and slowdown of cognitive decline despite the causal *PSEN1* mutation and high levels of amyloid beta pathology in the carrier[1]. However, the molecular effects enabling *E3*$^{S/S}$ mutation to confer protection remain unclear. Here, we replaced mouse Apoe with wild-type human *E3* or *E3*$^{S/S}$ on a tauopathy background. The *R136S* mutation markedly mitigated tau load and protected against tau-induced synaptic loss, myelin loss, and spatial learning. Additionally, the *R136S* mutation reduced microglial interferon response to tau pathology both *in vivo* and *in vitro*, suppressing cGAS-STING activation. Treating tauopathy mice carrying wild-type *E3* with cGAS inhibitor protected against tau-induced synaptic loss and induced similar transcriptomic alterations to those induced by the *R136S* mutation across brain cell types. Thus, cGAS-STING-IFN inhibition recapitulates the protective effects of *R136S* against tauopathy.

Keywords: APOE, microglia, cGAS, tauopathy, Christchurch, Alzheimer's, interferon

Introduction

Alzheimer's disease (AD) is the most prevalent form of dementia, characterized by pathological hallmarks of amyloid beta plaques and neurofibrillary tangles of hyperphosphorylated tau[2]. Amyloid pathology typically develops early in AD whereas tau pathology occurs later but correlates more accurately with AD progression and cognitive impairment[3-5]. Mutations on presenilin 1 (*PSEN1)* cause early onset autosomal dominant AD (ADAD) as early as 30-40 years of age[6]. The majority of AD patients have sporadic late-onset AD (LOAD), in which apolipoprotein E (APOE) is the predominant risk gene[7,8]. APOE is a lipid transporter expressed on astrocytes and microglia and has been shown to affect numerous microglial functions including neuroinflammation and phagocytosis[9-11]. The three major APOE variants, *APOE2*, *APOE3*, and *APOE4*, differ from each other at two amino acid positions, 112 and 158, and modulate AD risk. While *E3* is considered neutral, *E4* alleles elevate AD risk while *E2* reduces AD risk[12,13]. *E2* is associated with reduced amyloid toxicity. Additionally, the *APOE3*-Jacksonville mutation also appears to reduce amyloid toxicity[12].

A more recent study revealed that a patient carrying familial *PSEN1* E280A mutation was protected against cognitive decline until her 70s, attributed to her being homozygous for the *R136S* or Christchurch mutation on *APOE3* ($APOE3^{S/S}$)[1]. Despite her extraordinarily high amyloid burden, she exhibited low tau pathology in her frontal cortex and occipital cortex, typically vulnerable regions in AD[13], suggesting potent protective function of *R136S* mutation against tau-induced neurodegeneration. In mouse models, the *R136S* mutation was found to protect against tau pathology, neurodegeneration, and neuroinflammation on the *APOE4* background; this was in the well-characterized mouse model expressing *P301S* mutant tau, associated with Frontotemporal dementia (FTD)[14]. Additionally, $APOE3^{S/S}$ also protected against toxicity induced by inoculation of AD-tau in a transgenic amyloid mouse model[15]. Thus, even though the *R136S* mutation has only been identified in one patient thus far, the protective effects of *R136S* mutation are likely applicable to both *APOE3* and *APOE4* carriers, and such protection may extend to multiple diseases exhibiting tau pathology. Thus, dissecting the mechanisms enabling this mutation's protection could elucidate broad therapeutic implications.

Our current study aims to dissect the mechanisms underlying the protective function of $APOE3^{S/S}$ against tauopathy. We established human *APOE3* and $APOE3^{S/S}$ knockin models by replacing mouse *Apoe* with human *APOE3* and $APOE3^{S/S}$ cDNA, followed by crossing with *P301S* mice. We characterized the effects of $APOE3^{S/S}$ on tau pathology, and tau-induced spatial learning and memory deficits, and synaptic activity. We performed snRNA-seq to identify cell type-specific transcriptomic changes, and discovered that $APOE3^{S/S}$ reduced cGAS-STING-IFN signaling in microglia without affecting disease-associated microglial signatures (DAMs)[16] or microglial neurodegenerative phenotype (MGnD)[17]. We also

determined to what extent the protective function of the *R136S* mutation can be attributed to cGAS inhibition by treating *E3/P301S* mice with a cGAS inhibitor; using snRNA-seq, we compared cGAS inhibitor profiles with transcriptional signatures induced by *R136S* mutation across several cell types. Our study revealed an unexpected central role of cGAS-STING-IFN activation in opposing the *R136S* mutation-induced resilience.

Results

ApoE3$^{S/S}$ mutation protects against tau-induced spatial learning and memory impairment and rescues synaptic deficits.

To directly assess the effects of the *R136S* mutation on the *APOE3* background, we used CRISPR to insert human *APOE3* cDNA and *APOE3R136S* cDNA (*E3$^{S/S}$*) into the exon of the mouse *Apoe* locus, resulting in replacement of mouse Apoe with human *E3* or *E3$^{S/S}$* (**Fig. 1A**). PCR confirmed the correct recombination and insertion of human *E3* or *E3$^{S/S}$* cDNA at the *mApoe* locus (**Fig. S1 A–C**). We did not detect any nonspecific integration in the *E3* or *E3$^{S/S}$* lines. Sanger sequencing was performed to confirm the accuracy of the replacement (**Fig. S1 B, C**). We then crossed *E3* or *E3$^{S/S}$* mice with PS19 mice, which express the human MAPT transgene with *P301S* mutation (*P301S*), to study effects of *APOE3$^{S/S}$* on tau pathology in the absence of amyloid[16] (**Fig. 1A**). Interestingly, *E3$^{S/S}$* did not affect APOE levels in the frontal cortex or in plasma in the presence or absence of tau pathology (**Fig. S1 D-F**).

The *R136S* mutation delayed cognitive decline in the human carrier until she was in her 70s. We examined the effects of *E3$^{S/S}$* on tau-induced spatial learning deficits using the Morris Water Maze (MWM) test. At 9–10-months of age, tau failed to induce spatial learning deficits in female *E3 or E3$^{S/S}$ mice* (**Fig. 1B,C**), which is consistent in previous studies showing that female PS19 mice have weaker tau pathology and neurodegeneration in comparison to their male counterparts[26]. However, the spatial learning curve showed that 9–10-month-old *E3/P301S* male mice exhibited a significant delay, while no delay was observed in *E3$^{S/S}$/P301S* mice (**Fig. 1D, E**). In the probe trial performed at 24 hours, *E3$^{S/S}$/P301S* mice exhibited preference to the target quadrant, indicating preserved spatial memory (**Fig. 1F**). In contrast, no preference was observed in *E3/P301S* mice. Importantly, swim speeds were similar across all genotypes (**Fig. 1G**). Thus, *E3$^{S/S}$* ameliorated tau-induced spatial learning and memory.

To further dissect how *E3$^{S/S}$* affects network activity in tauopathy mice, we performed 16 channel local field potential (LFP) recordings in awake 6–7-month-old male mice exploring an open field chamber (**Fig. 1H**). We did not observe differences in the overall activity and speed in the open field among any experimental groups (**Fig. S2**). LFP recording measures amplitudes of oscillations across 0.5–250HZ (**Fig.**

1I). Both theta power (4–8 hz) and gamma power (30 to 100 Hz) are closely linked to key cognitive functions such as attention, memory, and consciousness, and were quantified in the somatosensory cortex, the visual cortex and the CA1 and dentate gyrus regions of the hippocampus (**Fig. 1J**). Consistent with the impaired learning and memory in *E3/P301S* mice, the amplitudes of theta power were significantly reduced. The tau-induced deficits were completely abolished on $E3^{S/S}$ background. *E3/P301S* mice also exhibited markedly reduced gamma power in the dentate gyrus (**Fig. 1J, K**). However, gamma power in the DG did not differ between $E3^{S/S}$ and $E3^{S/S}/P301S$ mice. Thus, both theta and gamma power were preserved in the hippocampal circuit in $E3^{S/S}/P301S$ mice (**Fig. 1J, K).**

***R136S* mutation on APOE3 protects against tau pathology and tau-induced synaptic loss.**

We next determined the effects of the *R136S* mutation on tau pathology by detecting pathogenic tau aggregates in 9–10-month-old *E3/P301S* and $E3^{S/S/}P301S$ male mice. Consistent with low tau load in the *R136S* human carrier, $E3^{S/S/}P301S$ mice exhibited a marked decrease in tau load across the hippocampus, including CA3 and CA1 subregions (**Fig 2. A–D**). To examine synaptic integrity of all four experimental groups, PSD95 immunoreactivity was measured in the CA1. We found that PSD95 immunofluorescence was significantly lower in *E3/P301S* mice compared with non-transgenic controls (**Fig 2. E,F**). However, this tau-induced synaptic loss was abolished on the $E3^{S/S}$ background (**Fig 2. E,F**).

Previous studies showed striking *APOE* isoform-specific effects on innate immune responses including microglia and astrocyte activation[11]. We next examined the effects of the *R136S* mutation on microgliosis and astrogliosis using IBA1 and GFAP staining respectively (**Fig 2**. **G-J**). IBA1 immunoreactivity was significantly elevated in *E3/P301S* mice, confirming tau-induced microgliosis, however the *R136S* mutation did not alter tau-induced microgliosis (**Fig 2. G-H**). Quantification of GFAP+ astrocytes revealed that tau induced similar increases in GFAP immunoreactivity on both *E3* and $E3^{S/S}$ backgrounds (**Fig 2. I-J**). Thus, the *R136S* mutation does not alter overall gliosis.

***R136S* mutation induces cell type-specific alterations across 6 CNS cell types in the presence of tau.**

To dissect the cell type-specific effects underlying protection by the *R136S* mutation, we then performed single nuclei RNA-seq (snRNA-seq) of hippocampi from male mice in all four genotypes (*E3, E3P301S,* $E3^{S/S}$, and $E3^{S/S}P301S$) at 9-10 months of age. 88,605 nuclei passed the stringent QC (**Fig. S3**). All major cell types were similarly represented across genotypes (**Fig. 3A, B**). The *R136S* mutation in tauopathy mice led to transcriptomic alterations in multiple cell types, including excitatory neurons (EN), inhibitory neurons (IN), astrocytes (AST), oligodendrocytes (OL), and microglia (MG) (**Fig S3, Table S1**). $E3^{S/S}$ altered gene expression in multiple cell types (**Fig. 3B**).

We investigated transcriptomic alterations and their downstream pathways in ENs. Top DEGs in ENs were highly enriched in genes involved in spliceosome assembly and function and RNA processing pathways, including *Srsf2*, *Srsf7*, and *Srsf11*, *Rbm25, Rbm39*, *Zranb2*, *Rsrp1*, *Luc7l3* & *Luc7l2* (**Fig. 3C**). Using gene set enrichment analysis (GSEA), we found that upregulated genes in ENs also were involved in nuclear structure and RNA processing (*Pnn*, *Pnisr*) (**Fig 3D**). Although fewer DEGs were observed in interneurons, the top pathways were also associated with RNA processing (**Fig 3F).** We then compared the top 50 up- and downregulated genes in both excitatory and inhibitory neurons and found an overwhelming number of splicing-related genes present in both cell types (**Fig 3G**). STRING analysis identified *Rbm25* as a central hub of these genes. To validate the reduction of *Rbm25* in *E3/P301S* compared to $E3^{S/S}$*/P301S*, we used immunohistochemistry to examine the co-localization of this splicing protein with NeuN, a marker for neurons. We found that *E3/P301S* mice had the lowest levels of RBM25 and NeuN colocalization compared to all other groups.

The *R136S* mutation also induced transcriptomic alterations in glial cells (**Table S1**). In astrocytes, the top gene downregulated in $E3^{S/S}$ astrocytes is Thioesterase Superfamily Member 4 (Them4), which regulates mitochondrial fatty acid metabolism and is involved in apoptotic process. It has been shown that Them4 regulates PI3K-AKT1 activity, which is involved in toxicity associated with AD risk allele TREM2[18-20] **(Fig. S4**). Another top downregulated gene in astrocytes is metabotropic glutamate receptor 5 (*Grm5*) (**Fig. S4**). Interestingly, blockade of *Grm5* in human astrocytes reduces pro-inflammatory responses to TNF-α and increases phagocytosis[21]. Among the top upregulated genes are prominent AD risk genes *Apoe* and *Clu*[22] (**Fig. S4**). *Clu* has been shown to exhibit astrocyte-derived synaptic and anti-amyloid qualities. For example, *Clu* overexpression in astrocytes rescued synaptic deficits in *Clu* knockout mice as well as an amyloid mouse model[23]. Other upregulated genes are involved in protective functions of astrocytes, such as a glial high-affinity glutamate transporter (*Slc1a2, Eaat2*), which plays a vital role in clearance of glutamate from synaptic clefts, preventing excitotoxicity and thereby protecting neurons[24] *(***Fig. S4***)*.

We also compared oligodendrocytes in *E3/P301S* and $E3^{S/S}$*P301S* hippocampi by performing pseudobulk analyses. The top upregulated genes include markers for mature oligodendrocytes including Myelin Oligodendrocyte Glycoprotein (*Mog)* and *Opalin*[25], consistent with a protective role of *R136S* mutation (**Fig. 4B, Table S1)**. More detailed subclustering analyses revealed that subcluster 2 (OL2) was significantly reduced by tau in *E3* but was preserved in $E3^{S/S}$ oligodendrocytes (**Fig. 4D, Table S2)**. Pathways upregulated by this subcluster were enriched in processes involved in sphingolipid synthesis, a primary component of myelin[26] (**Fig. 4E**). We then directly determined how *R136S* mutation affects demyelination associated with tauopathy (**Fig. 4G**). Immunostaining with anti-MBP revealed a tau-induced loss of MBP on the *E3* background, which did not occur on the $E3^{S/S}$ background (**Fig. 4H**). Therefore,

transcriptomic effects of the *R136S* mutation span multiple cell types and can result in protective outcomes such as myelin preservation.

***R136S* mutation specifically suppresses tau-induced cGAS-STING-IFN activation in microglia.**

Microglia play critical roles in mediating tau toxicity. We next examined how the *R136S* mutation affects microglial response to tau pathology in our snRNA-seq dataset (**Fig. 5A**). Microglia in *E3/P301S* and $E3^{S/S}$*/P301S* mice exhibited similar loss of microglial subcluster 1 (MG1) enriched with homeostatic markers (**Table S3**), and similar induction of MG2 enriched with disease-associated microglia (DAM) signature (**Fig. 5C, Table S3**). Indeed, the expression of canonical DAM genes was not distinguishable between *E3* and $E3^{S/S}$ in the presence of tau (**Fig 5D**). Pseudobulk analysis of global microglial changes revealed that genes involved in type-I interferon, including *Trim 30a*, *Cd300if, Ddx60, Stat1, Ifi204*, were among the top downregulated in $E3^{S/S}$*/P301S* microglia compared to *E3/P301S* counterparts (**Fig 5E, F**). Ingenuity pathway analyses were performed to examine upstream regulators. The top inhibited upstream regulators in $E3^{S/S}$*/P301S* microglia include EDN-1, and antiviral activators as cGAS and IFNA, and the top activated upstream regulators include those negatively involved in antiviral response such as TREX1, RNASEH2B, and those involved in mTOR and autophagy such as TSC1 (**Fig 5G**). We next performed immunostaining with STING, a downstream component of the cGAS pathway that stimulates interferon gene expression. Tau induced significant increases in microglial STING on *E3* background were completely abolished on $E3^{S/S}$ background (**Fig. 5H-I**).

***ApoE3*$^{S/S}$ suppresses tau-induced cGAS-STING-IFN response in a cell-autonomous manner.**

To determine if the $E3^{S/S}$ microglia downregulate interferon in a cell-autonomous manner, we isolated primary microglia from brains of *E3* and $E3^{S/S}$ pups and stimulated with recombinant tau (**Fig 6A**). We performed bulk RNA sequencing and found that the $E3^{S/S}$ primary microglia treated with tau continued to downregulate interferon genes, similar to what was shown *in vivo* via snRNAseq (**Fig 6B).** We then compared the top 50 up and downregulated genes in *E3* and $E3^{S/S}$ between *in vitro* and *in vivo* RNA sequencing; this comparison showed similar regulation patterns *in vitro* and *in vivo* (**Fig 6C, Table S4**). Then, we used GSEA to assess corresponding pathways in the primary microglia treated with tau (**Fig 6D**). We found that the top upregulated pathways in the $E3^{S/S}$ microglia were transcription regulator activity, RNA polymerase II transcription, negative regulation of RNA biosynthesis and apoptosis. The top downregulated pathways in the $E3^{S/S}$ microglia included IFN-gamma response, IFN-alpha response, innate immune response, and the defense response. Next, we used Ingenuity pathway analysis revealed STING1

and cGAS, as well as many other interferon related genes, as predicted upstream regulators in the *E3*$^{S/S}$ microglia (**Fig 5E**).

To determine if *E3*$^{S/S}$ microglia differ in their ability to uptake tau, we performed a tau chasing assay in which microglia were treated with tau, collected and replaced with fresh media at 2 hours and again at 24 hours (**Fig 5F**). We then immunolabeled for tau and found no significant difference in the amount of tau taken up by *E3* microglia at 2 hr timepoints. However, *E3*$^{S/S}$ microglia exhibited less intracellular tau at 24 hours than *E3* counterparts, suggesting a higher processing capacity (**Fig 5G, H**).

Inhibition of cGAS phenocopies transcriptomic alterations induced by *ApoE3*$^{S/S}$ and protects against tau-induced synaptic loss

Given that cGAS-STING-IFN is among the top downregulated pathways induced by the *R136S* mutation in microglia both *in vivo* and *in vitro*, we investigated whether pharmacological inhibition of the interferon response would phenocopy the effects induced by the *R136S* mutation. Our previous studies have established the efficacy of a brain permeable cGAS inhibitor (TDI6570) formulated in chow in protecting against tau-induced deficits in PS19 mice[13]. Similarly, 6-month-old *E3/P301S* mice were treated with control or cGASi-formulated diet for 3 months followed by snRNA-seq and assessment of synaptic integrity (**Fig. 7A-B**). We first examined cell type-specific transcriptomic changes in the hippocampus using snRNA-seq. 205,400 nuclei were analyzed after passing stringent QC (**Fig. S6**). All major cell types were similarly represented in all four genotypes (**Fig. 7A**). The *R136S* mutation in tauopathy mice led to transcriptomic alterations in multiple cell types, including excitatory neurons (EN), inhibitory neurons (IN), astroglia (AST), oligodendrocytes (OL), and microglia (MG) (**Fig 7B**).

We compared cell type-specific transcriptomic changes of *E3/P301S* mice induced by the cGASi chow versus those induced by *E3*$^{S/S}$ in the presence of tau pathology. Remarkably, out of the DEGs in microglia induced by either cGASi or R136S mutation, >50% were shared with a striking correlation ($R = 0.92$) (**Fig. 7C-D, Table S5**). Genes affected by both contexts include immune genes *Cd74* and *Cd84* as well as downregulation of several interferon genes including *Ifitm10*. Similarly striking overlap and correlation were observed in both INs ($R = 0.98$, **Fig. 7E,F, Table S5**) and ENs ($R = 0.96$, **Fig. 7G,H, Table S5**). These findings strongly support cGAS inhibition as one of major pathways induced by the *R136S* mutation in both neurons and microglia. In addition, cGAS inhibitor treatment ameliorated PSD95 reduction in *E3/P301S* tauopathy mice (**Fig. 7I-J**). Thus, cGAS inhibition is one of the key drivers of *R136S* mutation-induced resilience against tau toxicity.

DISCUSSION

Our current study combines functional assays, transcriptomic analyses, and pharmacological intervention to shed light on mechanisms enabling *E3*$^{S/S}$ to protect against tauopathy. We established new *APOE3* and *APOE3*$^{S/S}$ knock-in mice and demonstrated that the *E3*$^{S/S}$ mutation protects against tau-induced spatial learning deficits and declines in theta and gamma oscillations. Additionally, we observed that *E3*$^{S/S}$ mice exhibited a decreased tau load and tau-induced synaptic loss without affecting tau-induced microgliosis or astrogliosis. The *E3*$^{S/S}$ mutation affects multiple cell types including astrocytes, oligodendrocytes, neurons, and specifically downregulates cGAS/STING-IFN pathway in microglia. In primary microglia, the *E3*$^{S/S}$ mutation lowered tau retention and tau-induced IFN response, suggesting that microglial downregulation of the cGAS/STING-IFN pathway occurs cell-autonomously. Remarkably, treatment of a cGAS inhibitor to *E3/P301S* mice phenocopied the *E3*$^{S/S}$ mutation on microglial and neuronal transcriptomes and protected against tau-induced synaptic loss.

In our current model, we replaced mouse *Apoe* alleles with human *E3* and *E3*$^{S/S}$ cDNA. Consistent with the observation in an earlier study, in which genomic *APOE3* was used to replace mouse *Apoe* alleles, the *R136S* mutation does not affect brain APOE3 levels[27]. APOE isoforms were found to affect the steady-state levels of APOE in the brain, with ε2/2 >ε3/3 >ε4/4[28]. Lower levels of APOE4 were observed in both targeted replacement mice and human astrocytoma cultures, indicating a predisposition to enhanced degradation of APOE4 over APOE3 and APOE2, especially in astrocytes[28]. Increased systemic APOE levels have also been observed in carriers of the protective APOE2 isoform[15,29] while low levels of APOE have been associated with amyloid pathology and mild cognitive impairment in the clinic[30]. Furthermore, APOE isoforms have been shown to alter several of its functional characteristics such as HDL particle size, cholesterol efflux capacity, and acetyltransferase activity[31]. However, unlike Chen et al, which reported elevated plasma APOE levels in *E3*$^{S/S}$ mice, we observed similar APOE levels in *E3* and *E3*$^{S/S}$ mice in plasma. Importantly, APOE levels were not reported on the APOE4 background used in the Nelson et al study. Exactly how the *R136S* mutation affects APOE3 metabolism remains unclear. Nevertheless, the comparable APOE levels in the brain and plasma of our *E3* and *E3*$^{S/S}$ model allow us to investigate the specific effects induced by *R136S* mutation without the confounds caused by different levels of APOE isoforms.

Using both behavioral tests and LFP recording of network activities, we showed that *E3*$^{S/S}$ mice are protected against tau-induced deficits in spatial learning and memory deficits, as well as theta and gamma oscillations, in multiple brain regions. Notably, our analysis of network activity revealed that even early-stage tau pathology induced marked reduction of both theta and gamma power at 6-7 months of age, long before tau-induced neurodegeneration, supporting the notion that network dysfunction represents early

pathogenetic mechanisms in AD[32]. Previous studies have shown that amyloid pathology induces abnormal theta and gamma oscillations, likely due to deficient inhibitory interneuron activity, which we did not examine in this study[33-35]. The revelation that FTD tau pathology led to similar network dysfunction suggests converging network dysfunction in AD and primary tauopathies[36-38]. Indeed, gamma frequency modulation was found to be beneficial in models with either amyloid and/or tau pathology[39].

The *E3*$^{S/S}$ patient had lower tau load in comparison to others in her cohort with the PSEN1 mutation associated with ADAD and very high amyloid pathology[1]. We showed that *E3*$^{S/S}$*/P301S* mice demonstrated less tau pathology across the hippocampus, similar to the observations made on the *APOE4* background[14]. On the *E3* background, previous studies elucidated robust protective effects in tau pathology in the amyloid model induced by tau aggregates isolated from AD brains (AD-tau)[27]. Thus, while the protective effects of the *R136S* mutation were discovered on an *E3* carrier with amyloid pathology, it is likely that the protective mechanisms of the *R136S* mutation are broadly applicable, not only to both E3 and E4 carriers, but also could extend to FTLD-tau and primary tauopathies.

How does *R136S* mutation lower tau load? Previous studies point to neuronal or microglial mechanisms. So far, all *E3*$^{S/S}$ knockin models are whole-body knockin; conditional knockin models are needed to dissect the cell type-specific mechanisms. In primary microglia, we observed that *E3*$^{S/S}$ microglia have less intracellular tau at 24 hours than *E3* microglia, indicating more efficient tau processing and degradation, consistent with previous studies[27]. Our snRNA-seq analyses of excitatory and inhibitory neurons revealed striking upregulation of RNA-splicing pathways by the *R136S* mutation. Whether it is the consequence or causative of reduced tau load remains an open question.

The *R136S* mutation had a distinct effect on the transcriptomes of astrocytes, including upregulation of protective astrocytic genes, such as EAAT2, the main glutamate transporter that exerts protective function against excitotoxity. Its expression diminishes with age[40] and in postmortem brains of patients with sporadic AD correlates with signs of neuronal death[41]. Given that agonist of EAAT2 has been found to be neuroprotective[42], confirming and dissecting how the *R136S* mutation enhances expression of EAAT2 may be of therapeutic potential.

AD patients demonstrate exacerbated myelin loss[43,44]. Our findings indicate that the *R136S* mutation affects oligodendrocytes transcriptomes and protects against tau-induced myelin loss. Notably, APOE4 alone has also been shown to result in demyelination, even when tau pathology is absent[45]. Transcriptomic changes were also detected in an oligodendrocyte subpopulation on an E4 background with the *R136S* mutation[14]. Emerging evidence supports astrocytic signaling to oligodendrocytes plays a role in demyelination. For example, in human astrocytes, elevation of the AD risk allele CLU inhibited OPC proliferation and myelination while mounting an interferon response[46]. Taken together, oligodendrocytes

play a role in protection mediated by the *R136S* mutation, which may also be facilitated by cross-talk with other cell types.

Maladaptive microglia play a central role in pathological tau spread and tau toxicity[47,48]. While the exact toxic pathways remain elusive, several recent studies provide compelling evidence supporting interferon pathways to be particularly damaging, especially in the presence of tau pathology. In tauopathy mouse models, our previous studies suggest that the source of IFN signaling could be partially attributed to hyperactive cGAS-STING in tauopathy mice and the human AD brain[49]. *Cgas* deletion mitigated tauopathy-induced microglial IFN-I and protected against synapse loss, synaptic plasticity, and cognitive deficits[49]. Moreover, *APOE4* greatly exacerbates tau-induced neurodegeneration, partially attributed to a critical immune hub that involves IFN-driven microglial activation and interaction with cytotoxic T cells[50,51]. In contrast, our current study showed that the resilient $E3^{S/S}$ allele specifically suppresses tau-induced cGAS-STING-IFN signaling in microglia, without affecting DAM signature, which is unlike previous studies demonstrating that the *R136S* on the *E4* background downregulates disease-associated gene profiles across cell types[13]. Upon tau stimulation, $E3^{S/S}$ primary microglia exhibited lower expression of interferon-stimulated genes, suggesting a cell-autonomous effect of the *R136S* mutation in microglia. Previous studies have shown that the *R136S* mutation impairs APOE3's interaction with Heparan sulfate proteoglycans (HSPGs). In macrophages, HSPG was shown to fine tune inflammation via IFNb[52]. Specifically, macrophage HSPGs sequester IFNb and the degree of macrophage proteoglycan sulfation can determine and possibly predict disease outcomes of metabolic inflammatory respones[52]. Whether similar mechanisms are at play and how the impaired interaction of *R136S* with HSPG could lead to the suppression of IFN response in response to tau stimulation requires further investigation.

We lastly performed pharmacological inhibition of cGAS in *E3/P301S* mice to compare the protective effects induced by the chronic inhibition and those by the *R136S* mutation on the *E3* background. Indeed, the cGAS inhibitor induced protective effects against tau-induced synaptic loss, as expected from our previous studies in tauopathy mice on mouse *Apoe*. The remarkable overlap and striking correlation of the transcriptomic alteration across multiple cell types suggest that the resilience of the human carrier can be phenocopied through pharmacological inhibition of cGAS. Future studies elucidating the relationship between APOE isoforms and cGAS activation may prove useful in further understanding shared mechanisms and therapeutic potential of cGAS inhibitors in both ADRD and LOAD. Ultimately, our study sheds important light on the field to elucidate the *R136S* mutation's effect on tau-induced network activity and function, unravels the widespread transcriptomic effects of the *R136S* on neurons and glial cells, and unveils a potential therapeutic pathway to target.

ACKNOWLEDGEMENTS

The study was supported by: JPB Foundation (to LG), Tau Consortium (to LG), Cure Alzheimer Fund (to L.G), R01AG072758 (to LG), R01AG074541 (to LG), 1F32AG085960-01 (to SN), Gilliam Fellowship from Howard Hughes Institute (to CLL).

We would like to thank Ravi Kumar Nagiri for his assistance in producing TDI-6570 for use in this study. We would like to thank Guillermo Coronas-Samano for his help in setting up the behavioral suite and systems used for collection of Morris Water Maze data.

AUTHOR CONTRIBUTIONS

Conceptualization: LG, SN, ERT

Methodology: ERT, SG, SN, CLL, LG

Visualization: SN, CLL

Funding Acquisition: LG

Writing – original draft: SN, CLL, LG

Writing – reviewing and editing: LG, SN, CLL

DECLARATION OF INTERESTS

L.G is founder and equity holder of Aeton Therapeutics. S.S is consultant and equity holder of Aeton Therapeutics. L.G. and S.S. have filed a patent related to this work (Publication Number: WO/2023/154962, International Application No.: PCT/US2023/062593). The other authors declare no competing interest.

FIGURES

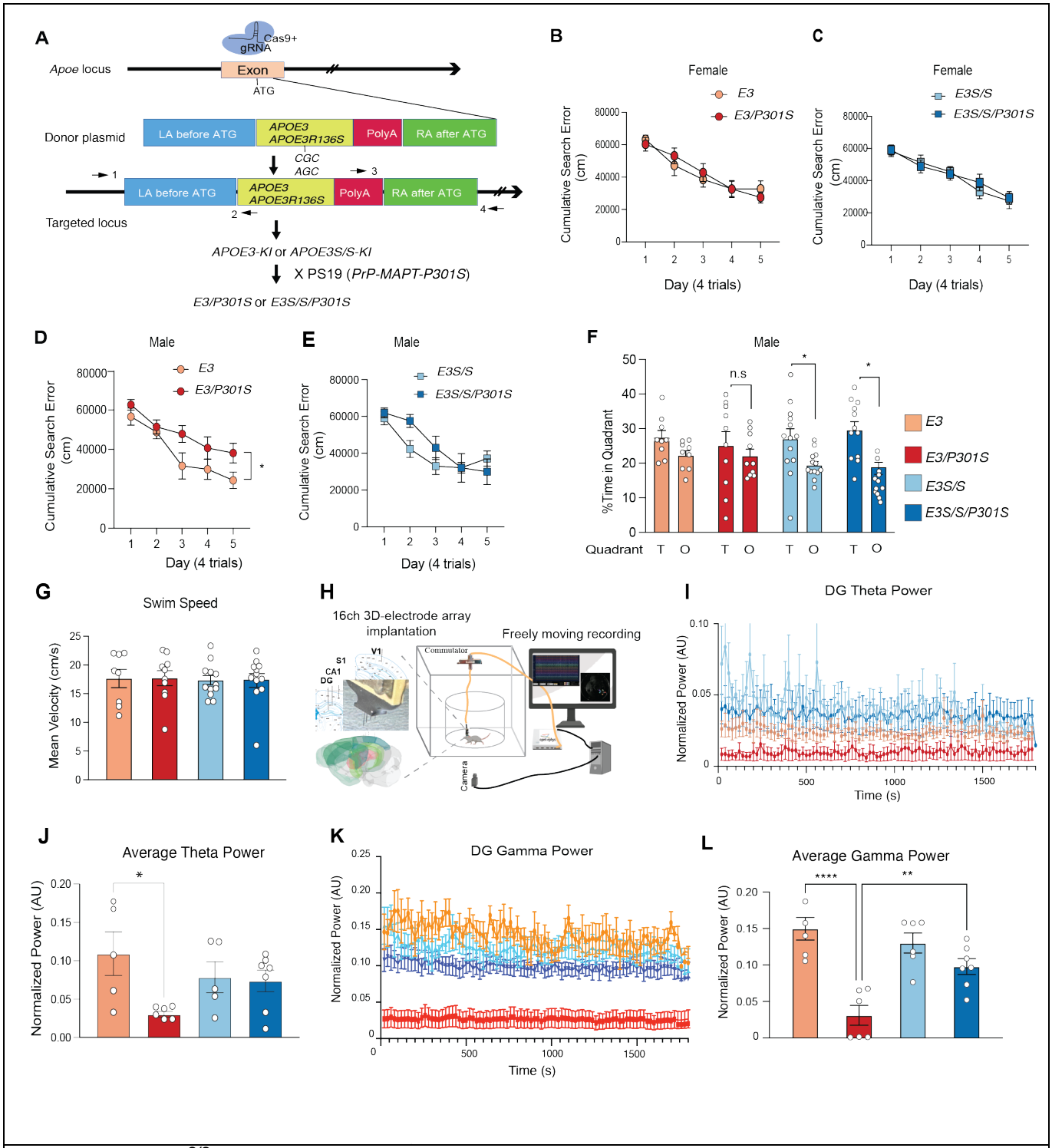

Figure 1. *ApoE3$^{S/S}$* mutation reduces tau-induced spatial learning and memory deficits and protects against reduced gamma power in the hippocampus.
(A) Schematic illustrating knockin of human *APOE3* on the mouse *Apoe* locus, insertion of *R136S* mutation, and cross with *P301S* mice.
(B) Cumulative search distance to target platform during hidden trials in a Morris water maze assessment of spatial learning and memory in 9-10 month old female *E3* and their *E3/P301S* mice, n= 10 for *E3* and N = 11 for *E3/P301S* mice. P= 0.5822. Data were analyzed by two-way ANOVA with Sidak's multiple comparison.

(C) Cumulative search distance to target platform during hidden trials in a Morris water maze assessment of spatial learning and memory in 9-10 month old female *E3*$^{S/S}$ and their *E3*$^{S/S}$*P301S* mice, n= 11 for both *E3* and *E3/P301S* groups, p = 0.8048. Data were analyzed by two-way ANOVA with Sidak's multiple comparison.
(D) Cumulative search distance to target platform during hidden trials in a Morris water maze assessment of spatial learning and memory in 9-10 month old male *E3* and their *E3/P301S* mice. N= 9 for *E3* and n= 10 for *E3/P301S*. *p= 0.0385. Data were analyzed by two-way ANOVA with Sidak's multiple comparison.
(E) Cumulative search distance in 9-10 month old male *E3*$^{S/S}$ and their *E3*$^{S/}$*S/P301S*. N= 13 for *E3* and n= 12 for *E3/P301S*. p= 0.4289. Data were analyzed by two-way ANOVA with Sidak's multiple comparison.
(F) Percentage of time spent in target (T) or the average time spent in the nontarget (others; O) quadrants during the 24 hour probe in the Morris Water Maze assessment. n = 9 for *E3*, n= 10 for *E3/P301S*, n= 13 for *E3*$^{S/S}$, n= 12 for *E3*$^{S/S}$*/P301S*; p= 0.0547, 0.625, 0.0574 and 0.0161 respectively. Data were analyzed by two-tailed t-test and Wilcoxon matched-pairs signed rank test. *, p < 0.05.
(G) Swim speeds were unaltered across all genotypes. n = 8 for *E3*, n= 10 for *E3/P301S*, n= 13 for *E3*$^{S/S}$, n= 12 for *E3*$^{S/S}$*P301S*; p= 0.999. Data were analyzed two-way ANOVA with main effects model.
(H) Schematic of local field potential (LFP) recordings in male 6-7 month old mice in open field chamber.
(I) Average theta power from DG in all four experimental groups showing a marked reduction in *E3/P301S* mice in comparison to all other groups.
(J) Quantification of average theta power in all brain regions showing reduction in *E3/P301S* mice in comparison to all other groups. N= 5 for *E3*, n=6 for *E3/P301S, n*= 5 for *E3*$^{S/S}$, n= 7 *E3*$^{S/S}$*/P301S*. *p<0.05. Data were analyzed by two-way ANOVA with mixed-effects model.
(K) Average gamma power from DG in all four experimental groups showing a marked reduction in *E3P301S* mice in comparison to all other groups.
(L) Quantification of average DG gamma power across all four groups. N= 5 for *E3*, n=6 for *E3/P301S, n*= 5 for *E3*$^{S/S}$, n= 7 *E3*$^{S/S}$*/P301S*. ****p<0.0001. Data were analyzed by two-way ANOVA with mixed-effects model.

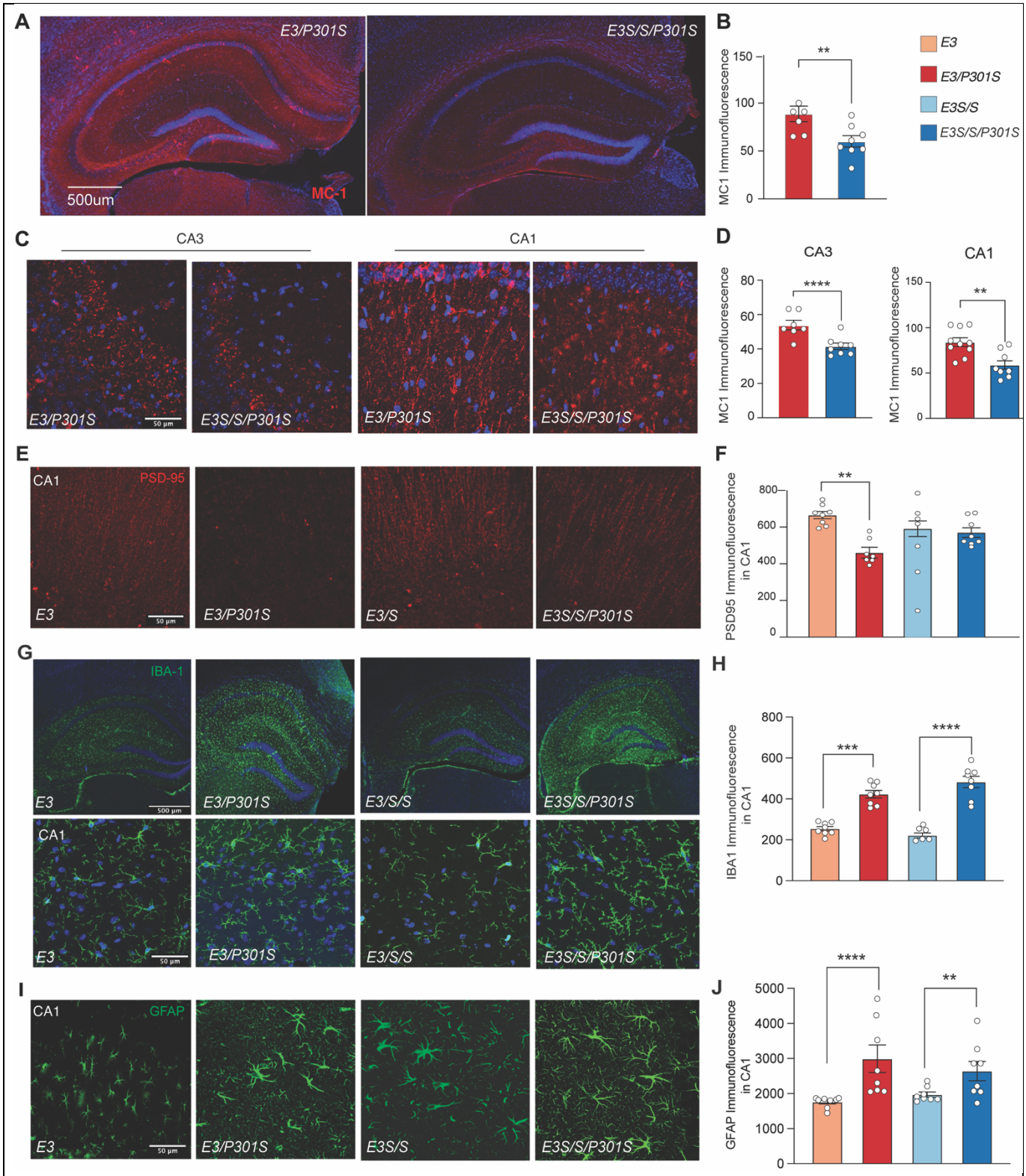

Figure 2: *ApoE3$^{S/S}$* decreases hippocampal tau inclusions and prevents tau-induced synaptic density loss.

(A) Representative immunofluorescence images of whole hippocampus of *E3/P301S* and *E3$^{S/S}$/P301S* mice labeled with MC-1 (red); scale bar, 500um.

(B) Quantification of MC-1 immunofluorescence intensities, showing decreased MC-1 throughout *E3$^{S/S}$/P301S* mice. Results are presented as average intensity measures from 3-4 sections per animal

with 8 animals/experimental group. Data are reported as mean ± SEM. ****p<0.0001. Data were analyzed by two-way ANOVA with mixed-effects model.
(C) Representative immunofluorescence images of CA3 and CA1 subregions of hippocampus of *E3/P301S* and *E3$^{S/S}$/P301S* mice respectively labeled with MC-1 (red); scale bar, 50um.
(D) Quantification of MC-1 immunofluorescence intensities, showing decreased MC-1 throughout *E3$^{S/S}$/P301S* mice in both subregions. Results are presented as average intensity measures from 3-4 sections per animal with 8 animals/experimental group. Data are reported as mean ± SEM. **p= 0.0019 and ****p<0.0001 for CA3 and CA1 respectively. Data were analyzed by two-way ANOVA with mixed-effects model.
(E) Representative immunofluorescence images of CA1 subregion of hippocampus of *E3/P301S* and *E3$^{S/S}$/P301S* mice respectively labeled with PSD-95 (red); scale bar, 50um.
(F) Quantification of PSD-95 immunofluorescence intensities, showing decreased PSD-95 throughout *E3$^{S/S}$/P301S* mice in both subregions. Results are presented as average intensity measures from 3-4 sections per animal with 8 animals/experimental group. Data are reported as mean ± SEM. ****p<0.0001 for *E3* compared to *E3/P301S*, p=0.9551 for *E3$^{S/S}$* compared to *E3$^{S/S}$/P301S*. Data were analyzed by two-way ANOVA with mixed-effects model.
(G) Representative immunofluorescence images of whole hippocampus and CA1 subregion of hippocampus of *E3/P301S* and *E3$^{S/S}$/P301S* mice respectively labeled with Iba-1 (green); scale bar, 500um and 50um respectively.
(H) Quantification of Iba1 immunofluorescence intensities, showing increased Iba-1 in both *P301S* groups. Results are presented as average intensity measures from 3-4 sections per animal with 8 animals/experimental group. Data are reported as mean ± SEM. ***p=0.0003 for *E3* compared to *E3/P301S*, ****p<0.0001 for *E3$^{S/S}$* compared to *E3$^{S/S}$/P301S*. Data were analyzed by two-way ANOVA with mixed-effects model.
(I) Representative immunofluorescence images of CA1 subregion of hippocampus of *E3/P301S* and *E3$^{S/S}$P301S* mice respectively labeled with GFAP (green); scale bar, 50um respectively.
(J) Quantification of GFAP immunofluorescence intensities, showing increased GFAP in both *P301S* groups. Results are presented as average intensity measures from 3-4 sections per animal with 8 animals/experimental group. Data are reported as mean ± SEM. ****p=0.0001 for *E3* compared to *E3/P301S* and **p=0.0014 for *E3$^{S/S}$* compared to *E3$^{S/S}$/P301S*. Data were analyzed by two-way ANOVA with mixed-effects model.

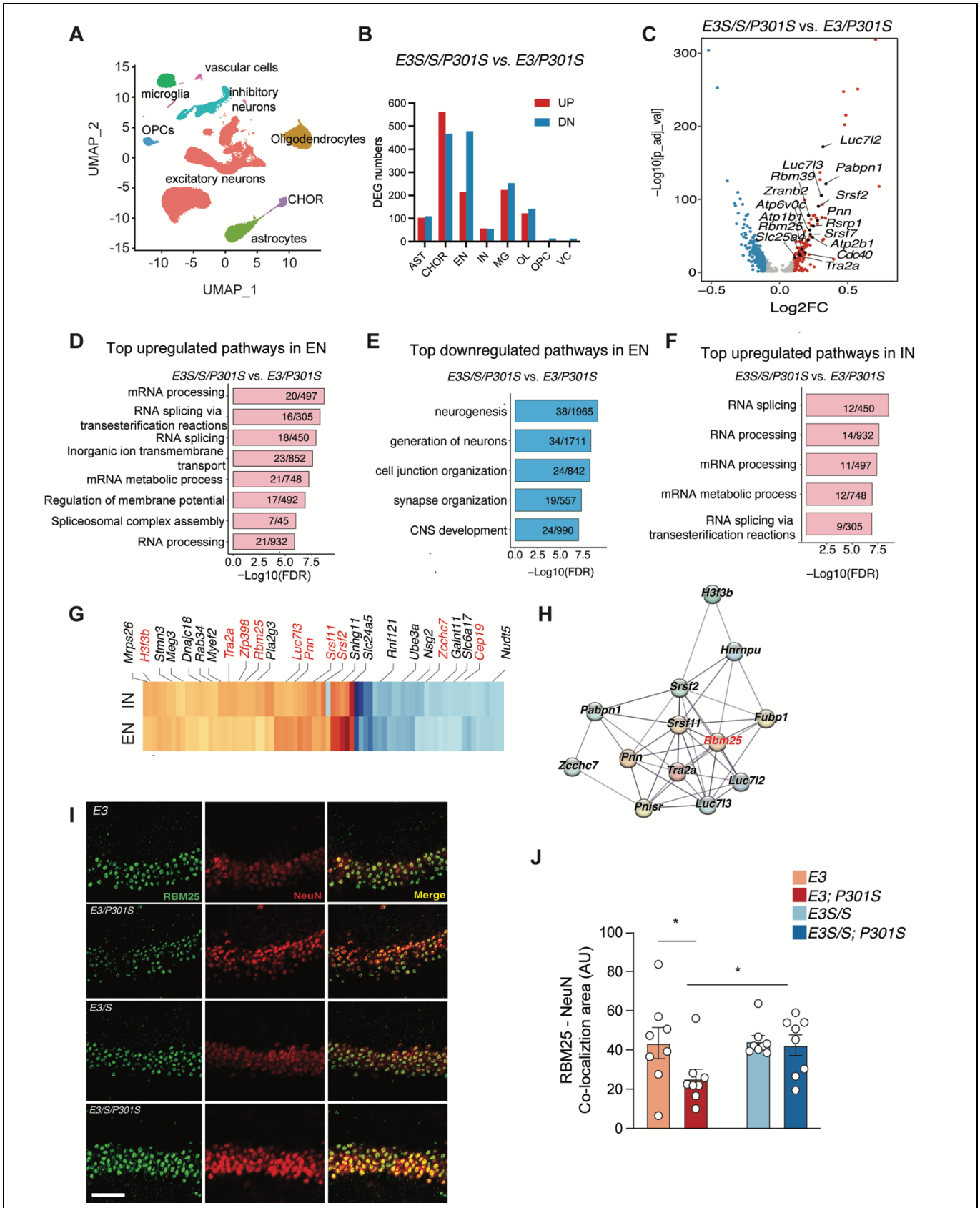

Figure 3. *R136S* mutation alters RNA processing pathways in ENs and INs in *E3/P301S* mice.
(A) UMAP of 8 detected cell types using single nuclei RNA-sequencing of the hippocampi from 9–10-month-old *E3* and *E3$^{S/S}$* mice with or without *P301S* tau, n=3 mice in each genotype.
(B) Number of significant DEGs between *E3$^{S/S}$* and *E3* in the presence of tau.

(C) Volcano plot of DEGs in excitatory neurons between *E3$^{S/S}$/P301S* and *E3/P301S*. Dashed lines represent log2foldchange threshold of 0.1 and adjusted p value threshold of 0.05.
(D–E) Top upregulated (D) and downregulated (E) pathways (*E3$^{S/S}$/P301S* vs. *E3/P301S*) in ENs.
(F) Top upregulated pathways (*E3$^{S/S}$/P301S* vs. *E3/P301S*) in INs.
(G) Heatmap showing overlapping top 50 upregulated and top 50 downregulated genes, sorted by average logFC in excitatory neurons and inhibitory neurons.
(H) String analysis showing RNA splicing related genes in neurons.
(I) Representative images of colocalization of RBM25 and NEUN immunofluorescence across each genotype.
(J) Quantification of colocalization of RBM25 and NEUN signal across genotypes, n=8 mice per genotype with 2-3 sections per mouse. Data are reported as mean ± SEM and analyzed via two-way ANOVA with mixed effects model. *p<0.05.

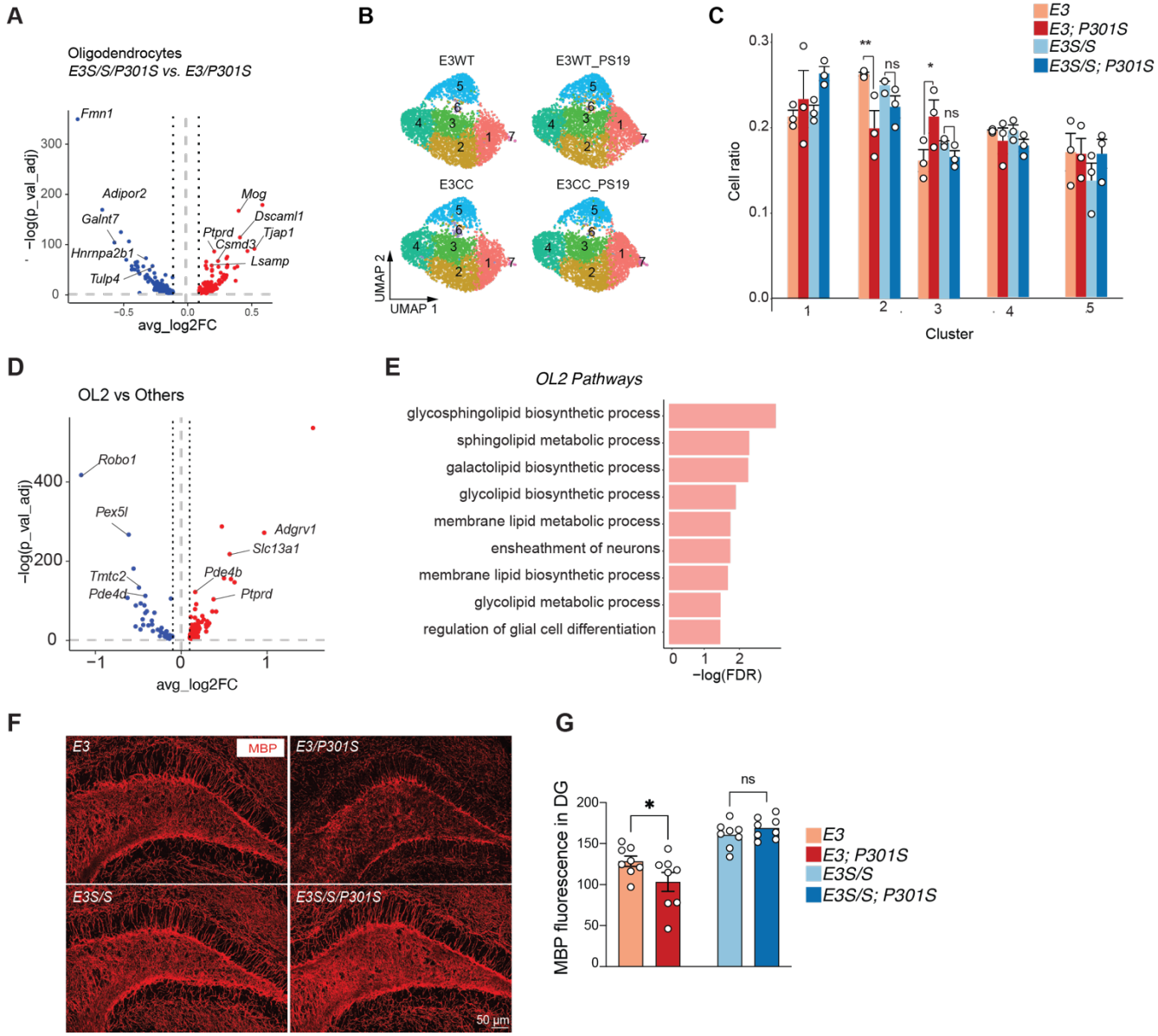

Figure 4: *ApoE3$^{S/S}$* induces cell type-specific transcriptomic changes in oligodendrocytes and protects against tau-induced myelin loss.
(A) Volcano plot of DEGs in oligodendrocytes between *E3$^{S/S}$/P301S* and *E3/P301S*. Dashed lines represent log2foldchange threshold of 0.1 and adjusted p value threshold of 0.05.
(B) UMAP of oligodendrocyte subclusters split by genotype.
(C) Quantification of cell ratios within each subcluster.

(D) Volcano plot of oligodendrocyte cluster 2 markers. Dashed lines represent log2foldchange threshold of 0.1 and adjusted p value threshold of 0.05.
(E) Gene ontology pathway analysis of upregulated oligodendrocytes DEGs *E3$^{S/S}$/P301S* vs. *E3/P301S.*
(F) Representative images of immunofluorescence for MBP across each genotype.
(G) Quantification of MBP signal across genotypes, n=8 mice per genotype with 3-4 sections per mouse. Data in are reported as mean ± SEM and analyzed via two-way ANOVA with mixed effects model. *$p<0.05$, **$p<0.01$.

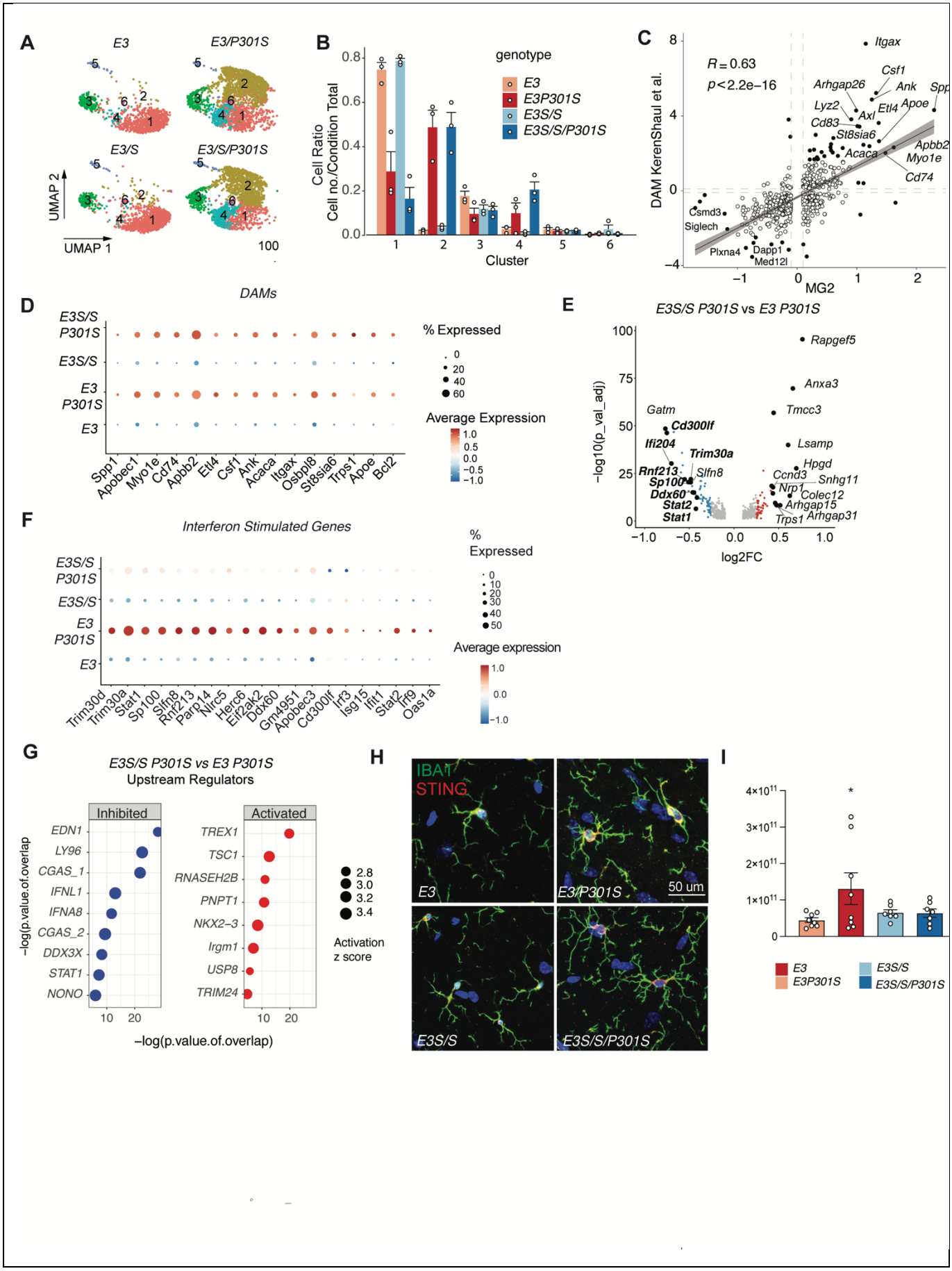
A
E3
E3/P301S
E3/S
E3/S/P301S
UMAP 2
UMAP 1
100
B
genotype
E3
E3P301S
E3S/S
E3S/S/P301S
Cell Ratio
Cell no./Condition Total
Cluster
C
R = 0.63
p < 2.2e−16
DAM KerenShaul et al.
MG2
Itgax
Csf1
Arhgap26
Ank
Spp
Lyz2
Etl4
Apoe
Axl
Cd83
St8sia6
Apbb2
Acaca
Myo1e
Cd74
Csmd3
Siglech
Plxna4
Dapp1
Med12l
D
DAMs
E3S/S P301S
E3S/S
E3 P301S
E3
% Expressed
Average Expression
Spp1
Apobec1
Myo1e
Cd74
Apbb2
Etl4
Csf1
Ank
Acaca
Itgax
Osbpl8
St8sia6
Trps1
Apoe
Bcl2
E
E3S/S P301S vs E3 P301S
−log10(p_val_adj)
log2FC
Rapgef5
Anxa3
Gatm
Tmcc3
Cd300lf
Ifi204
Trim30a
Lsamp
Hpgd
Rnf213
Slfn8
Ccnd3
Snhg11
Sp100
Nrp1
Ddx60
Colec12
Stat2
Arhgap15
Stat1
Trps1
Arhgap31
F
Interferon Stimulated Genes
% Expressed
Average expression
Trim30d
Trim30a
Stat1
Sp100
Slfn8
Rnf213
Parp14
Nlrc5
Herc6
Eif2ak2
Ddx60
Gm4951
Apobec3
Cd300lf
Irf3
Isg15
Ifit1
Stat2
Irf9
Oas1a
G
E3S/S P301S vs E3 P301S
Upstream Regulators
Inhibited
Activated
EDN1
LY96
CGAS_1
IFNL1
IFNA8
CGAS_2
DDX3X
STAT1
NONO
TREX1
TSC1
RNASEH2B
PNPT1
NKX2−3
Irgm1
USP8
TRIM24
−log(p.value.of.overlap)
Activation z score
H
IBA1
STING
E3
E3/P301S
50 um
E3S/S
E3S/S/P301S
I
E3
E3P301S
E3S/S
E3S/S/P301S

Figure 5. *ApoE$^{S/S}$* specifically abolishes tau-induced cGAS-STING-IFN response in microglia.
(A) UMAP of 6,762 microglia split by genotype
(B) Quantification of cell ratios within each subcluster.
(C) Correlation between microglia cluster 2 gene expression and published DAM gene signature from Keren Shaul et al.
(D) Dotplot DAM gene expression by genotype
(E) Volcano plot of DEGs in excitatory neurons between *E3$^{S/S}$/P301S* and *E3/P301S* thresholded by log2foldchange >0.1 or <-0.1 and adjusted p value threshold of 0.05.
(F) Dotplot of interferon gene expression by genotype
(G) Upstream regulators identified by Ingenuity Pathway Analysis for both up- and downregulated genes.
(H) Representative immunofluorescence images of CA1 subregion of hippocampus of *E3, E3/P301S, E3$^{S/S}$, E3$^{S/S}$/P301S* groups co-labeled with Iba1 (green) and STING (red); scale bar, 50um.
(I) Quantification of co-localized integrated density of STING in IBA1+ cells. Results are presented as average intensity measures from 3-4 sections per animal with 8 animals/genotype. *p=0.0363 for *E3* compared to *E3/P301S*. Data in (B), (I) are reported as mean ± SEM. Data in (I) were analyzed by two-way ANOVA with mixed-effects model.

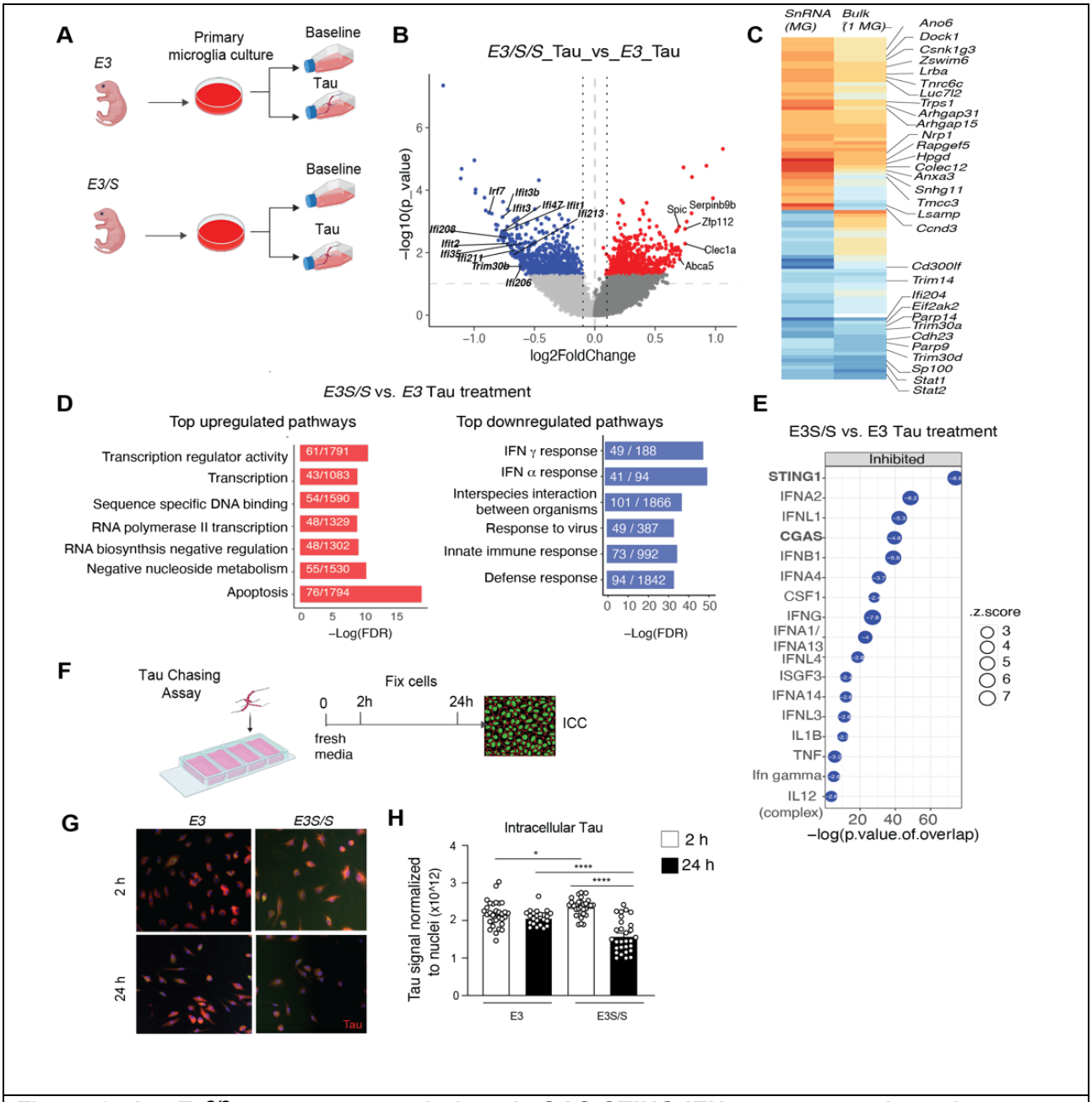

Figure 6. *ApoE3$^{S/S}$* suppresses tau-induced cGAS-STING-IFN response and accelerates tau processing in primary microglia.

(A) Schematic of treatment plan for primary microglia isolated from either *E3* or *E3$^{S/S}$* pups cultured with basal media or treated with tau fibrils.

(B) Volcano plot of DEGs in primary microglia between *E3$^{S/S}$* + tau and *E3 + tau* thresholded by log2foldchange >0.1 or <-0.1 and p value threshold of 0.05 showing downregulation of interferon genes in bold.

(C) Heatmap showing top 50 upregulated and 50 downregulated genes by log fold change in tau-stimulated *E3$^{S/S}$* versus *E3* primary microglia compared to those in *E3$^{S/S}$/P301S* mice.

(D) Top upregulated and downregulated pathways in tau-stimulated *E3$^{S/S}$* versus *E3* primary microglia using GSEA.

(E) Top predicted upstream inhibitors in tau-stimulated *E3$^{S/S}$* versus *E3* primary microglia showing STING and cGAS in bold.

(F) Schematic for tau chasing assay experiment.

(G) Representative immunofluorescence images of *E3* and *E3*$^{S/S}$ microglia at 2 hours and 24 hours following tau treatment. Red: anti-tau antibody
(H) Quantification of tau immunolabeling in red fluorescence normalized to number of nuclei/image in *E3* and *E3*$^{S/S}$ microglia at 2 hours and 24 hours. Each point on graph represents one well of a chamber slide, with 4-5 images taken/slide. 3 biological replicates and 8 technical replicates were completed. Data is reported as mean +/- SEM, and analyzed with two-way ANOVA with mixed effects model. *p=0.0228 for *E3* compared to *E3*$^{S/S}$ at 2 hours, ****p<0.0001 for *E3*$^{S/S}$ compared to 2 hours compared to 24 hours, and ****p<0.0001 for *E3* compared to *E3*$^{S/S}$ at 24 hours.

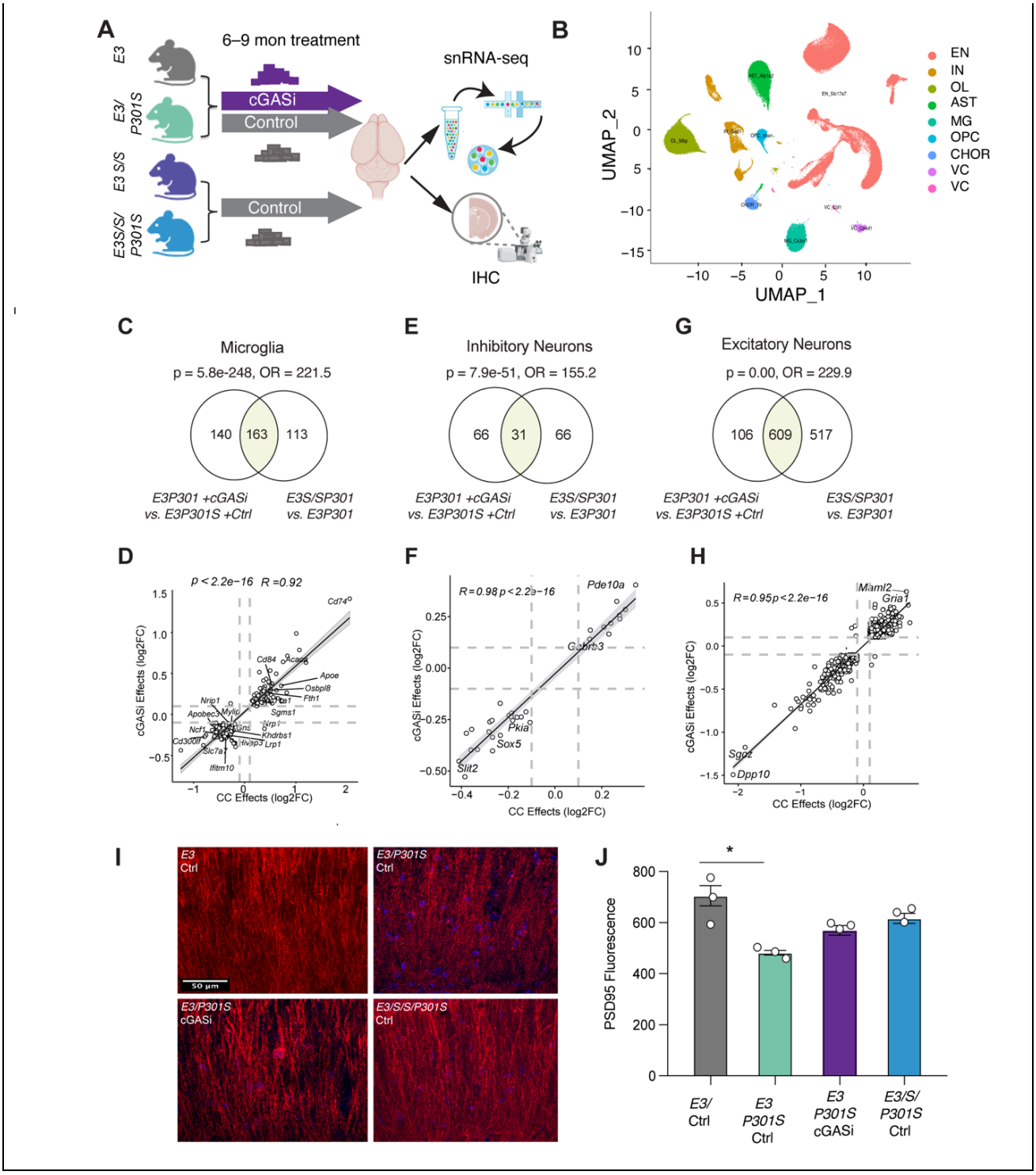

Fig 7. cGAS inhibition mimics transcriptomic effects of *R136S* mutation across brain cell types.

(A) Schematic of treatment plan for *E3* and *E3*$^{S/S}$ mice treated with either control diet or cGAS inhibitor diet at 6 months of age for 3 month duration.

(B) UMAP of detected cell types in snRNA-seq dataset

(C) Venn diagram showing unique effect of cGAS (left) in comparison to effect of *R136S* mutation (right) in microglia as well as overlapping genes between the effects (middle, highlighted in green).

(D) Correlation of gene expression for overlapping genes in (C).

(E) Venn diagram showing unique effect of cGAS (left) in comparison to effect of *R136S* mutation (right) in inhibitory neurons as well as overlapping genes between the effects (middle, highlighted in green).

(F) Correlation of gene expression for overlapping genes in (E).

(G) Venn diagram showing unique effect of cGAS (left) in comparison to effect of *R136S* mutation (right) in excitatory neurons as well as overlapping genes between the effects (middle, highlighted in green).

(H) Correlation of gene expression for overlapping genes in (G).

(I) Representative immunofluorescence images of PSD95 staining in CA1 subregion of hippocampus of *E3* mice treated with control diet, *E3P301S* mice treated with control diet, *E3P301S* mice treated with cGAS inhibitor diet, and *E3*$^{S/S}$*P301S* mice treated with control diet. (J) Quantification of PSD95 immunofluorescence intensity for the corresponding conditions in (I), n=4 animals with 3-4 sections per mouse. Data are reported as mean ± SEM. Data in (J) were analyzed by two-way ANOVA with mixed-effects model, *$p<0.05$.

MATERIALS/METHODS

Generating Mouse Line

To introduce a human *APOE3 and APOE3Christchurch (APOE3-R136S, E3S/S)* cDNA into mouse *Apoe* genetic locus, a donor plasmid was designed and made. The human *APOE3* or*APOE3S/S* cDNA and a poly A tail were flanked by left and right homology arms which were designed to insert human *APOE3* or *APOE3S/S* right before the start codon of mouse *Apoe* gene. Upon recombination, the mouse *Apoe* promoter and regulatory elements would drive expression of the inserted human *APOE3* or*APOE3S/S* cDNA, whereas the expression of mouse *Apoe* gene would be inactivated. A single guide RNA (sgRNA) was selected. RNP containing sgRNA and Cas9 protein was prepared. Pronuclear injections of RNP and the donor plasmid was performed at the Rockefeller University transgenic core facility. Genomic DNA from founders was isolated from tail lysate. To screen the specific knockin mice, two PCR amplifications were performed with primers flanking the outside of the homology arms and on the human APOE3 transgene. The PCR products were sequenced to validate the correct insertion and the locus integrity. Non-specific integration of the donor DNA was characterized by two simple PCR amplifications using two sets of primers on the backbone of the plasmids.

To distinguish homozygous from heterozygous mice, tail DNA from F2 offspring was further characterized by PCR with three primers, two primers on the targeting genomic sequences and one primer on the transgene. Three independent *APOE3* or *APOE3S/S* lines were generated. One *APOE3* or *APOE3S/S* line was used to cross with a transgenic mouse model overexpressing human tau harboring the P301S mutation to evaluate the effect of APOE3 Christchurch on tau pathology. Mice were maintained in barrier facility with 12-hour light, 12-hour dark cycle and stable temperature conditions.

Tissue collection

Mice were euthanized using FatalPlus and perfused with cold PBS following cardiac puncture for blood collection. Blood was collected in EDTA-coated tubes and spun down to isolate plasma. After complete perfusion, left hemibrain was fixed in formalin for 24-48 hours followed by storage in 30% sucrose. Right hemibrain was microdissected for hippocampus and frontal cortex, which were frozen in dry ice and stored at -80°C until further processing.

Immunohistochemistry

Fixed hemibrain was sectioned in 30 um-thick sections via microtome and stored in cryoprotectant. 3-5 hippocampal sections were picked per animal and following rinses with PBST, underwent antigen retrieval using Reveal Decloaker (Biocare Medical). Sections were incubated overnight at 4 degrees in

primary antibodies: PSD-95 (Millipore, 1:400), IBA-1 (Abcam, 1:400), STING (Cell Signaling, 1:200), NeuN (Millipore, 1:200), MC-1 (Gift from Peter Davies lab, 1:2500), GFAP (Abcam, 1:500). Following Alexafluor secondary antibody incubation at 1:500, sections were rinsed with PBST and mounted using Prolong Gold Anti-Fade reagent with DAPI. Slides were sealed with clear nail polish and kept at 4°C. Immunofluorescence was visualized using either LSM880 laser scanning confocal microscope and 3-4 images per animal were captured at 40X in CA1 and CA3 regions of hippocampus. Whole hippocampal images were taken at 10X with 11-13 planes and 2x2 images were stitched. After image capture, images were separated by color channel and underwent background subtraction and thresholding. Signal intensity was measured via ImageJ. Intensity of 1-2 control sections stained only with secondary antibody was averaged and subtracted from all sections. Signal intensity was normalized to area, averaged across sections for each animal, and plotted in Prism. Experimenters performing imaging and quantification were blinded.

Single nuclei RNA sequencing

Nuclei isolation from frozen mouse hippocampi was adapted from a previous study [Habib 2017], with modifications. All procedures were performed on ice or at 4°C. In brief, postmortem brain tissue was placed in 1,500 µl of Sigma nuclei PURE lysis buffer (Sigma, NUC201-1KT) and homogenized with a Dounce tissue grinder (Sigma, D8938-1SET) with 15 strokes with pestle A and 15 strokes with pestle B. The homogenized tissue was filtered through a 35-µm cell strainer, centrifuged at 600g for 5 min at 4 °C and washed three times with 1 ml of PBS containing 1% bovine serum albumin (BSA, Thermo Fisher Scientific, 37525), 20 mM DTT (Thermo Fisher Scientific, 426380500) and 0.2 U μl^{-1} recombinant RNase inhibitor (Ambion, AM2684). Nuclei were then centrifuged at 600g for 5 min at 4 °C and resuspended in 350 µl of PBS containing 0.04% BSA and 1× DAPI, followed by fluorescence-activated cell sorting to remove cell debris. The sorted suspension of DAPI-stained nuclei was counted and diluted to a concentration of 1,000 nuclei per µl in PBS containing 0.04% BSA.

For droplet-based snRNA-seq, libraries were prepared with Chromium Single Cell 3′ Reagent Kits v3 (10x Genomics, PN-1000075) according to the manufacturer's protocol. The snRNA-seq libraries were sequenced on a NovaSeq 6000 sequencer (Illumina) with 100 cycles.

Gene counts were obtained by aligning reads to the mm10 genome with Cell Ranger software (v.3.1.0; 10x Genomics). To account for unspliced nuclear transcripts, reads mapping to pre-mRNA were counted. Cell Ranger 3.1.0 default parameters were used to call cell barcodes. We further removed genes expressed in no more than three cells, cells with unique gene counts over 4,000 or less than 300, cells with UMI counts over 20,000 and cells with a high fraction of mitochondrial reads (>5%). Potential doublet cells were predicted using DoubletFinder for each sample separately, with high-confidence doublets removed. Normalization

and clustering were done with the Seurat package v3.2.2 (Stuart, Butler 2019). In brief, counts for all nuclei were scaled by the total library size multiplied by a scale factor (10,000) and transformed to log space. A set of 2,000 highly variable genes was identified with SCTransform from the sctransform R packageFindVariableFeatures function with vst method. This returned a corrected unique molecular identifier count matrix, a log-transformed data matrix and Pearson residuals from the regularized negative binomial regression model. Principal-component analysis was done on all genes, and t-distributed stochastic neighbor embedding was run on the top 15 principal components. Cell clusters were identified with the Seurat functions FindNeighbors (using the top 15 principal components) and FindClusters (resolution = 0.1). In this analysis, the neighborhood size parameter pK was estimated using the mean variance-normalized bimodality coefficient (BCmvn) approach, with 15 principal components used and pN set as 0.25 by default. Sample integration was performed using FindIntegrationAnchors and IntegrateData functions in Seurat. For the baseline *E3, E3P301S, E3$^{S/S}$ and E3$^{S/S}$P301S* cohort snRNAseq, we sequenced 3 hippocampi/group. For the TDI-treated cohort, we also sequenced 3 hippocampi/group for the following groups: *E3/control diet, E3$^{S/S}$/control diet, E3P301S/control diet, E3$^{S/S}$P301S/control diet, E3/TDI, E3$^{S/S}$/TDI, E3P301S/TDI.* For each cluster, we assigned a cell-type label using statistical enrichment for sets of marker genes and manual evaluation of gene expression for small sets of known marker genes. Differential gene expression analysis was done using the FindMarkers function and MAST (Finak 2015). To identify gene ontology and pathways enriched in the DEGs, DEGS were analyzed using the MSigDB gene annotation database (Subramanian 2005, Liberzon 2011). To control for multiple testing, we used the Benjamini–Hochberg approach to constrain the FDR.

Western blot

25 ug frontal cortex or hippocampal lysate prepared above were boiled for 5 minutes and run on 26-well 4-12% Bis-Tris gels (Invitrogen) using MES buffer (Invitrogen) for 1 hour. Proteins were transferred from gel onto PVDF membrane for 2 hours. Membranes were washed three times for 10 min each in TBS with 0.01% triton X-100 (TBST). Membranes were blocked for 30 minutes in 5% milk in TBST and incubated with APOE (1:800, CalBiochem) and GAPDH (1:1,000, GeneTex) antibodies overnight in cold room. The following day, membranes were washed three times for 10 min each in TBST and incubated in appropriate HRP secondary for 1 hour, rinsed, and followed by ECL development and imaging using Bio-Rad imager.

Electrophysiological recording in freely moving mice

All experimental procedures were approved by the Weill Cornell Medical College Animal Care and Use Committee following National Institutes of Health guideline. Mice were initially anesthetized with 3.5 %

isoflurane mounted on a stereotaxic frame and tmaintained under ~1.2% isoflurane**.** Body temperature was maintained at 37 °C with a regulated heating blanket (World Precision Instruments, Sarasota, FL). A craniotomy was drilled for electrode insertion. Animals were implanted with a custom 16-ch 3D electrode array (Kedou Brain-Computer Technology, Suzhou, China) that contains 4 tetrodes over somatosensory (S1), the CA1 of hippocampus, dentate gyrus (DG), and primary visual cortex (V1) (S1 : antero-posterior (AP) -1.8mm, mediolateral (ML) 2.3mm , dorsoventral (DV) 1.0mm, CA1: AP -1.8mm, ML 1.5mm, DV1.4 mm, DG: AP -1.8mm, ML 1.0mm, DV 2.0mm, V1: AP -3.0mm, ML 2.3mm, DV 0.6mm. Fig xA). Stainless steel screws were implanted into the skull to provide electrical ground and mechanical stability for drives and the whole construct was bonded to the skull using C&B-Metabond luting cement (Parkell, Edgewood, NY). Two weeks after implantation, animals were put in a circular open field chamber (8228, Pinnacle Technology, Lawrence, KS) to record spontaneous activity continuously for 30 min. Electrophysiological data were acquired using an Intan RHD eadstage (Intan Technologies, LA, CA) and the Open Ephys acquisition board and software (OEPS, Alges, Portugal) sampled at 30kHz[53]. Locomotion was simultaneously acquired with a FLIR camera (Teledyne FLIR, North Billerica, MA) and the open-source Bonsia software[54] recording at 50 Hz.

Local field potential analysis

The offline LFP analysis was performed using custom-written Matlab script (MathWorks, Natick, MA). Briefly, LFP data will be preprocessed by first applying an anti-aliasing lowpass (<400Hz) zero-phase 8-order Chebyshev Type I filter then downsampling to 1000Hz. The power of theta (4-10 Hz) and gamma (30-90 Hz) were calculated then averaged by each tetrode to obtain the low and high band oscillation activity from each brain region. The normalized power was converted from the above value by dividing the average 10 sec baseline value at resting state when mice didn't show any movement in the behavior video. The averaged power for the entire open filed session was also calculated for the group comparison. Markless pose estimation for locomotion measurement will be performed by deep learning based DeeLabCut from the behavioral video data set[55].

Primary microglial culture

Primary microglial cells were collected from mouse pups at postnatal days 1–3. Briefly, the brain cortices were isolated and minced. Tissues were dissociated in 0.25% Trypsin-EDTA for 10 min at 37 °C and agitated every 5 min. Two hundred microliters of DNAse I (Millipore) was then added. Trypsin was neutralized with complete medium (DMEM; Thermo Fisher) supplemented with 10% heat-inactivated FBS (Hyclone), and tissues were filtered through 70-μm cell strainers (BD Falcon) and pelleted by centrifugation

at 250*g*. Mixed glial cultures were maintained in growth medium at 37 °C and 5% CO_2 for 7–10 d *in vitro*. Once bright, round cells began to appear in the mixed glial cultures, recombinant mouse granulocyte–macrophage colony-stimulating factor (1 ng ml^{-1}; Life Technologies) was added to promote microglia proliferation. Primary microglial cells were collected by mechanical agitation after 48–72 h and plated on poly-D-lysine-coated 24-well plates (Corning) in growth medium. Microglia were maintained in DMEM supplemented with 10% FBS, 100 U ml^{-1} penicillin and 100 μg ml^{-1} streptomycin. At 24 hours after plating, microglia were treated with 1ug/ml of ON4R.

Bulk sequencing analysis

Primary microglia isolated from *E3* and $E3^{S/S}$ pups were isolated and treated with tau as described above and collected 24 hours later. Total RNA was extracted from the samples using QuickRNA MicroPrep Kit (Zymo Research). After RNA isolation, total RNA integrity was checked using a 2100 Bioanalyzer (Agilent Technologies), and concentrations were measured by Nanodrop (Thermo Fisher. RNA was isolated from microglia using the Quick-RNA MicroPrep Kit (Zymo Research, R1051). RNA was shipped to Novogene for library preparation and bulk RNA sequencing. Differential gene expression was analyzed with the DESeq2 1.38.3 package131. Counts were normalized using the median of ratios method. Genes with <15 counts across all samples were excluded from analysis. To control for multiple testing, we used the Benjamini–Hochberg approach to constrain the FDR. Pathway analysis was done using the MSigDB gene annotation database. Ingenuity Pathway Analysis (QIAGEN, Inc.) was used to identify gene activation networks and upstream regulators. Raw read counts per gene were extracted using HTSeq-count v0.11.2[59].

Morris Water Maze

Mice were assessed for spatial learning and memory in the Morris Water Maze during the light cycle. Briefly, mice were placed in a circular pool (122cm in diameter, blue polyethylene, made by Maze Engineers) filled with water made with non-toxic chalk. Mice were trained to locate a submerged 10cm-wide circular platform 1cm below the surface of the water during 4 training trials per day for 5 days. Training trials were split into 2 sessions, morning and afternoon, which were 3-4 hours apart. Trials within each session were 8-10min apart. If mice did not find the platform within 60s, they were gently guided to the platform by the experimenter. After each trial, each mouse was placed into an empty cage lined with paper towels to dry off before being returned to the home cage. On the 6th day, spatial memory was tested by removing the platform for the probe trial. To decrease anxiety-like behavior and avoid glare on the camera, the room was kept to 40-45 lux. All trials were recorded using Noldus Ethovision XT software v.16

(Leesburg, VA, USA). Trials were manually checked for errors with tracking. Cumulative distance to the platform ("Search Error"), swim velocity (cm/s), and total distance swam were calculated using Ethovision for all trials. Probe trials were also assessed for time spend in the target quadrant versus the average of time spent in the non-target quadrants and the number of times the target location was crossed.

Y Maze

Male and female mice were tested separately. Mice were placed into the center of the y-maze (each arm width: 5cm, length: 35 cm, height: 20cm, custom built) and allowed to explore for 10min to measure hippocampal-based short-term memory. Trials were recorded using Noldus Ethovision XT v.16 (Leesburg, VA, USA), and scored for the number of arm entries and spontaneous alterations by an experimenter.

REFRERENCES

1. Arboleda-Velasquez, J.F., Lopera, F., O'Hare, M., Delgado-Tirado, S., Marino, C., Chmielewska, N., Saez-Torres, K.L., Amarnani, D., Schultz, A.P., Sperling, R.A., et al. (2019). Resistance to autosomal dominant Alzheimer's disease in an APOE3 Christchurch homozygote: a case report. Nat Med *25*, 1680-1683. 10.1038/s41591-019-0611-3.
2. Hardy, J., and Selkoe, D.J. (2002). The amyloid hypothesis of Alzheimer's disease: Progress and problems on the road to therapeutics. Science *297*, 353–356.
3. Malpetti, M., Joie, R., and Rabinovici, G.D. (2022). Tau Beats Amyloid in Predicting Brain Atrophy in Alzheimer Disease: Implications for Prognosis and Clinical Trials. J Nucl Med *63*, 830-832. 10.2967/jnumed.121.263694.
4. Lee, J.C., Kim, S.J., Hong, S., and Kim, Y. (2019). Diagnosis of Alzheimer's disease utilizing amyloid and tau as fluid biomarkers. Exp Mol Med *51*, 1-10. 10.1038/s12276-019-0250-2.
5. Bloom, G.S. (2014). Amyloid-beta and tau: the trigger and bullet in Alzheimer disease pathogenesis. JAMA Neurol *71*, 505-508. 10.1001/jamaneurol.2013.5847.
6. De Strooper, B., Saftig, P., Craessaerts, K., Vanderstichele, H., Guhde, G., Annaert, W., Von Figura, K., and Van Leuven, F. (1998). Deficiency of presenilin-1 inhibits the normal cleavage of amyloid precursor protein. Nature *391*, 387–390.
7. Mahley, R.W., Weisgraber, K.H., and Huang, Y. (2006). Apolipoprotein E4: a causative factor and therapeutic target in neuropathology, including Alzheimer's disease. Proc Natl Acad Sci U S A *103*, 5644-5651.
8. Holtzman, D.M., Bales, K.R., Tenkova, T., Fagan, A.M., Parsadanian, M., Sartorius, L.J., Mackey, B., Olney, J., McKeel, D., Wozniak, D., and Paul, S.M. (2000). Apolipoprotein E isoform-dependent amyloid deposition and neuritic degeneration in a mouse model of Alzheimer's disease. Proc Natl Acad Sci U S A *97*, 2892-2897. 10.1073/pnas.050004797.
9. Lee, S., Devanney, N.A., Golden, L.R., Smith, C.T., Schwartz, J.L., Walsh, A.E., Clarke, H.A., Goulding, D.S., Allenger, E.J., Morillo-Segovia, G., et al. (2023). APOE modulates microglial immunometabolism in response to age, amyloid pathology, and inflammatory challenge. Cell Rep *42*, 112196. 10.1016/j.celrep.2023.112196.
10. Wang, N., Wang, M., Jeevaratnam, S., Rosenberg, C., Ikezu, T.C., Shue, F., Doss, S.V., Alnobani, A., Martens, Y.A., Wren, M., et al. (2022). Opposing effects of apoE2 and apoE4 on microglial activation and lipid metabolism in response to demyelination. Mol Neurodegener *17*, 75. 10.1186/s13024-022-00577-1.

11. Shi, Y., Yamada, K., Liddelow, S.A., Smith, S.T., Zhao, L., Luo, W., Tsai, R.M., Spina, S., Grinberg, L.T., Rojas, J.C., et al. (2017). ApoE4 markedly exacerbates tau-mediated neurodegeneration in a mouse model of tauopathy. Nature *549*, 523-527. 10.1038/nature24016.
12. Liu, C.C., Murray, M.E., Li, X., Zhao, N., Wang, N., Heckman, M.G., Shue, F., Martens, Y., Li, Y., Raulin, A.C., et al. (2021). APOE3-Jacksonville (V236E) variant reduces self-aggregation and risk of dementia. Sci Transl Med *13*, eabc9375. 10.1126/scitranslmed.abc9375.
13. Sepulveda-Falla, D., Sanchez, J.S., Almeida, M.C., Boassa, D., Acosta-Uribe, J., Vila-Castelar, C., Ramirez-Gomez, L., Baena, A., Aguillon, D., Villalba-Moreno, N.D., et al. (2022). Distinct tau neuropathology and cellular profiles of an APOE3 Christchurch homozygote protected against autosomal dominant Alzheimer's dementia. Acta Neuropathol. 10.1007/s00401-022-02467-8.
14. Nelson, M.R., Liu, P., Agrawal, A., Yip, O., Blumenfeld, J., Traglia, M., Kim, M.J., Koutsodendris, N., Rao, A., Grone, B., et al. (2023). The APOE-R136S mutation protects against APOE4-driven Tau pathology, neurodegeneration and neuroinflammation. Nat Neurosci *26*, 2104-2121. 10.1038/s41593-023-01480-8.
15. Chen, Y., Song, S., Parhizkar, S., Lord, J., Zhu, Y., Strickland, M.R., Wang, C., Park, J., Tabor, G.T., Jiang, H., et al. (2023). APOE3ch alters microglial response and suppresses Abeta-induced tau seeding and spread. Cell. 10.1016/j.cell.2023.11.029.
16. Keren-Shaul, H., Spinrad, A., Weiner, A., Matcovitch-Natan, O., Dvir-Szternfeld, R., Ulland, T.K., David, E., Baruch, K., Lara-Astaiso, D., Toth, B., et al. (2017). A Unique Microglia Type Associated with Restricting Development of Alzheimer's Disease. Cell *169*, 1276-1290 e1217. 10.1016/j.cell.2017.05.018.
17. Krasemann, S., Madore, C., Cialic, R., Baufeld, C., Calcagno, N., El Fatimy, R., Beckers, L., O'Loughlin, E., Xu, Y., Fanek, Z., et al. (2017). The TREM2-APOE Pathway Drives the Transcriptional Phenotype of Dysfunctional Microglia in Neurodegenerative Diseases. Immunity *47*, 566-581 e569. 10.1016/j.immuni.2017.08.008.
18. Parcellier, A., Tintignac, L.A., Zhuravleva, E., Cron, P., Schenk, S., Bozulic, L., and Hemmings, B.A. (2009). Carboxy-Terminal Modulator Protein (CTMP) is a mitochondrial protein that sensitizes cells to apoptosis. Cell Signal *21*, 639-650. 10.1016/j.cellsig.2009.01.016.
19. Ono, H., Sakoda, H., Fujishiro, M., Anai, M., Kushiyama, A., Fukushima, Y., Katagiri, H., Ogihara, T., Oka, Y., Kamata, H., et al. (2007). Carboxy-terminal modulator protein induces Akt phosphorylation and activation, thereby enhancing antiapoptotic, glycogen synthetic, and glucose uptake pathways. Am J Physiol Cell Physiol *293*, C1576-1585. 10.1152/ajpcell.00570.2006.
20. Sayed, F.A., Kodama, L., Fan, L., Carling, G.K., Udeochu, J.C., Le, D., Li, Q., Zhou, L., Wong, M.Y., Horowitz, R., et al. (2021). AD-linked R47H-TREM2 mutation induces disease-enhancing microglial states via AKT hyperactivation. Sci Transl Med *13*, eabe3947. 10.1126/scitranslmed.abe3947.
21. de Lima, I.B.Q., Cardozo, P.L., Fahel, J.S., Lacerda, J.P.S., Miranda, A.S., Teixeira, A.L., and Ribeiro, F.M. (2023). Blockade of mGluR5 in astrocytes derived from human iPSCs modulates astrocytic function and increases phagocytosis. Front Immunol *14*, 1283331. 10.3389/fimmu.2023.1283331.
22. Balcar, V.J., Zeman, T., Janout, V., Janoutová, J., Lochman, J., and Šerý, O. (2021). Single Nucleotide Polymorphism rs11136000 of CLU Gene (Clusterin, ApoJ) and the Risk of Late-Onset Alzheimer's Disease in a Central European Population. Neurochem Res *46*, 411-422. 10.1007/s11064-020-03176-y.
23. Chen, F., Swartzlander, D.B., Ghosh, A., Fryer, J.D., Wang, B., and Zheng, H. (2021). Clusterin secreted from astrocyte promotes excitatory synaptic transmission and ameliorates Alzheimer's disease neuropathology. Mol Neurodegener *16*, 5. 10.1186/s13024-021-00426-7.
24. Yang, Y., Gozen, O., Watkins, A., Lorenzini, I., Lepore, A., Gao, Y., Vidensky, S., Brennan, J., Poulsen, D., Won Park, J., et al. (2009). Presynaptic regulation of astroglial excitatory neurotransmitter transporter GLT1. Neuron *61*, 880-894. 10.1016/j.neuron.2009.02.010.
25. Jiang, W., Yang, W., Yang, W., Zhang, J., Pang, D., Gan, L., Luo, L., Fan, Y., Liu, Y., and Chen, M. (2013). Identification of Tmem10 as a novel late-stage oligodendrocytes marker for detecting hypomyelination. Int J Biol Sci *10*, 33-42. 10.7150/ijbs.7526.
26. Giussani, P., Prinetti, A., and Tringali, C. (2021). The role of Sphingolipids in myelination and myelin stability and their involvement in childhood and adult demyelinating disorders. J Neurochem *156*, 403-414. 10.1111/jnc.15133.

27. Chen, Y., Song, S., Parhizkar, S., Lord, J., Zhu, Y., Strickland, M.R., Wang, C., Park, J., Tabor, G.T., Jiang, H., et al. (2023). APOE3ch alters microglial response and suppresses Aβ-induced tau seeding and spread. Cell. 10.1016/j.cell.2023.11.029.
28. Riddell, D.R., Zhou, H., Atchison, K., Warwick, H.K., Atkinson, P.J., Jefferson, J., Xu, L., Aschmies, S., Kirksey, Y., Hu, Y., et al. (2008). Impact of apolipoprotein E (ApoE) polymorphism on brain ApoE levels. J Neurosci *28*, 11445-11453. 10.1523/JNEUROSCI.1972-08.2008.
29. Nakamura, T., Kawarabayashi, T., Ueda, T., Shimomura, S., Hoshino, M., Itoh, K., Ihara, K., Nakaji, S., Takatama, M., Ikeda, Y., and Shoji, M. (2023). Plasma ApoE4 Levels Are Lower than ApoE2 and ApoE3 Levels, and Not Associated with Plasma Abeta40/42 Ratio as a Biomarker of Amyloid-beta Amyloidosis in Alzheimer's Disease. J Alzheimers Dis *93*, 333-348. 10.3233/JAD-220996.
30. Aslam, M.M., Fan, K.H., Lawrence, E., Bedison, M.A., Snitz, B.E., DeKosky, S.T., Lopez, O.L., Feingold, E., and Kamboh, M.I. (2023). Genome-wide analysis identifies novel loci influencing plasma apolipoprotein E concentration and Alzheimer's disease risk. Mol Psychiatry *28*, 4451-4462. 10.1038/s41380-023-02170-4.
31. Hong, B.V., Zheng, J., Agus, J.K., Tang, X., Lebrilla, C.B., Jin, L.W., Maezawa, I., Erickson, K., Harvey, D.J., DeCarli, C.S., et al. (2022). High-Density Lipoprotein Changes in Alzheimer's Disease Are APOE Genotype-Specific. Biomedicines *10*. 10.3390/biomedicines10071495.
32. Palop, J.J., and Mucke, L. (2010). Amyloid-beta-induced neuronal dysfunction in Alzheimer's disease: from synapses toward neural networks. Nat Neurosci *13*, 812-818. nn.2583 [pii]

10.1038/nn.2583 [doi].
33. Busche, M.A., and Konnerth, A. (2015). Neuronal hyperactivity--A key defect in Alzheimer's disease? Bioessays *37*, 624-632. 10.1002/bies.201500004.
34. Fu, H., Rodriguez, G.A., Herman, M., Emrani, S., Nahmani, E., Barrett, G., Figueroa, H.Y., Goldberg, E., Hussaini, S.A., and Duff, K.E. (2017). Tau Pathology Induces Excitatory Neuron Loss, Grid Cell Dysfunction, and Spatial Memory Deficits Reminiscent of Early Alzheimer's Disease. Neuron *93*, 533-541 e535. 10.1016/j.neuron.2016.12.023.
35. Verret, L., Mann, E.O., Hang, G.B., Barth, A.M., Cobos, I., Ho, K., Devidze, N., Masliah, E., Kreitzer, A.C., Mody, I., et al. (2012). Inhibitory interneuron deficit links altered network activity and cognitive dysfunction in Alzheimer model. Cell *149*, 708-721. 10.1016/j.cell.2012.02.046.
36. Hijazi, S., Heistek, T.S., Scheltens, P., Neumann, U., Shimshek, D.R., Mansvelder, H.D., Smit, A.B., and van Kesteren, R.E. (2020). Early restoration of parvalbumin interneuron activity prevents memory loss and network hyperexcitability in a mouse model of Alzheimer's disease. Mol Psychiatry *25*, 3380-3398. 10.1038/s41380-019-0483-4.
37. Algamal, M., Russ, A.N., Miller, M.R., Hou, S.S., Maci, M., Munting, L.P., Zhao, Q., Gerashchenko, D., Bacskai, B.J., and Kastanenka, K.V. (2022). Reduced excitatory neuron activity and interneuron-type-specific deficits in a mouse model of Alzheimer's disease. Commun Biol *5*, 1323. 10.1038/s42003-022-04268-x.
38. Xu, Y., Zhao, M., Han, Y., and Zhang, H. (2020). GABAergic Inhibitory Interneuron Deficits in Alzheimer's Disease: Implications for Treatment. Front Neurosci *14*, 660. 10.3389/fnins.2020.00660.
39. Iaccarino, H.F., Singer, A.C., Martorell, A.J., Rudenko, A., Gao, F., Gillingham, T.Z., Mathys, H., Seo, J., Kritskiy, O., Abdurrob, F., et al. (2016). Gamma frequency entrainment attenuates amyloid load and modifies microglia. Nature *540*, 230-235. 10.1038/nature20587.
40. Sharma, A., Kazim, S.F., Larson, C.S., Ramakrishnan, A., Gray, J.D., McEwen, B.S., Rosenberg, P.A., Shen, L., and Pereira, A.C. (2019). Divergent roles of astrocytic versus neuronal EAAT2 deficiency on cognition and overlap with aging and Alzheimer's molecular signatures. Proc Natl Acad Sci U S A *116*, 21800-21811. 10.1073/pnas.1903566116.
41. Masliah, E., Alford, M., DeTeresa, R., Mallory, M., and Hansen, L. (1996). Deficient glutamate transport is associated with neurodegeneration in Alzheimer's disease. Ann Neurol *40*, 759-766. 10.1002/ana.410400512.

42. Kong, Q., Chang, L.C., Takahashi, K., Liu, Q., Schulte, D.A., Lai, L., Ibabao, B., Lin, Y., Stouffer, N., Das Mukhopadhyay, C., et al. (2014). Small-molecule activator of glutamate transporter EAAT2 translation provides neuroprotection. J Clin Invest *124*, 1255-1267. 10.1172/JCI66163.
43. Zhan, X., Jickling, G.C., Ander, B.P., Liu, D., Stamova, B., Cox, C., Jin, L.W., DeCarli, C., and Sharp, F.R. (2014). Myelin injury and degraded myelin vesicles in Alzheimer's disease. Curr Alzheimer Res *11*, 232-238. 10.2174/1567205011666140131120922.
44. Nasrabady, S.E., Rizvi, B., Goldman, J.E., and Brickman, A.M. (2018). White matter changes in Alzheimer's disease: a focus on myelin and oligodendrocytes. Acta Neuropathol Commun *6*, 22. 10.1186/s40478-018-0515-3.
45. Blanchard, J.W., Akay, L.A., Davila-Velderrain, J., von Maydell, D., Mathys, H., Davidson, S.M., Effenberger, A., Chen, C.Y., Maner-Smith, K., Hajjar, I., et al. (2022). APOE4 impairs myelination via cholesterol dysregulation in oligodendrocytes. Nature *611*, 769-779. 10.1038/s41586-022-05439-w.
46. Liu, Z., Chao, J., Wang, C., Sun, G., Roeth, D., Liu, W., Chen, X., Li, L., Tian, E., Feng, L., et al. (2023). Astrocytic response mediated by the CLU risk allele inhibits OPC proliferation and myelination in a human iPSC model. Cell Rep *42*, 112841. 10.1016/j.celrep.2023.112841.
47. Asai, H., Ikezu, S., Tsunoda, S., Medalla, M., Luebke, J., Haydar, T., Wolozin, B., Butovsky, O., Kugler, S., and Ikezu, T. (2015). Depletion of microglia and inhibition of exosome synthesis halt tau propagation. Nat Neurosci *18*, 1584-1593. 10.1038/nn.4132.
48. Wang, C., Fan, L., Khawaja, R.R., Liu, B., Zhan, L., Kodama, L., Chin, M., Li, Y., Le, D., Zhou, Y., et al. (2022). Microglial NF-κB drives tau spreading and toxicity in a mouse model of tauopathy. Nat Commun *13*, 1969. 10.1038/s41467-022-29552-6.
49. Udeochu, J.C., Amin, S., Huang, Y., Fan, L., Torres, E.R.S., Carling, G.K., Liu, B., McGurran, H., Coronas-Samano, G., Kauwe, G., et al. (2023). Tau activation of microglial cGAS-IFN reduces MEF2C-mediated cognitive resilience. Nat Neurosci *26*, 737-750. 10.1038/s41593-023-01315-6.
50. Shi, Y., Yamada, K., Liddelow, S.A., Smith, S.T., Zhao, L., Luo, W., Tsai, R.M., Spina, S., Grinberg, L.T., Rojas, J.C., et al. (2017). ApoE4 markedly exacerbates tau-mediated neurodegeneration in a mouse model of tauopathy. Nature *549*, 523-527. 10.1038/nature24016.
51. Chen, X., Firulyova, M., Manis, M., Herz, J., Smirnov, I., Aladyeva, E., Wang, C., Bao, X., Finn, M.B., Hu, H., et al. (2023). Microglia-mediated T cell infiltration drives neurodegeneration in tauopathy. Nature *615*, 668-677. 10.1038/s41586-023-05788-0.
52. Gordts, P., Foley, E.M., Lawrence, R., Sinha, R., Lameda-Diaz, C., Deng, L., Nock, R., Glass, C.K., Erbilgin, A., Lusis, A.J., et al. (2014). Reducing macrophage proteoglycan sulfation increases atherosclerosis and obesity through enhanced type I interferon signaling. Cell Metab *20*, 813-826. 10.1016/j.cmet.2014.09.016.
53. Siegle, J.H., López, A.C., Patel, Y.A., Abramov, K., Ohayon, S., and Voigts, J. (2017). Open Ephys: an open-source, plugin-based platform for multichannel electrophysiology. Journal of Neural Engineering *14*, 045003. 10.1088/1741-2552/aa5eea.
54. Lopes, G., and Monteiro, P. (2021). New Open-Source Tools: Using Bonsai for Behavioral Tracking and Closed-Loop Experiments. Frontiers in Behavioral Neuroscience *15*. 10.3389/fnbeh.2021.647640.
55. Mathis, A., Mamidanna, P., Cury, K.M., Abe, T., Murthy, V.N., Mathis, M.W., and Bethge, M. (2018). DeepLabCut: markerless pose estimation of user-defined body parts with deep learning. Nature Neuroscience *21*, 1281-1289. 10.1038/s41593-018-0209-y.
56. Martin, M. (2011). Cutadapt Removes Adapter Sequences From High-Throughput Sequencing Reads. EMBnet.journal *17*, 10-12. doi.org/10.14806/ej.17.1.200.
57. Dobin, A., Davis, C.A., Schlesinger, F., Drenkow, J., Zaleski, C., Jha, S., Batut, P., Chaisson, M., and Gingeras, T.R. (2013). STAR: ultrafast universal RNA-seq aligner. Bioinformatics *29*, 15-21. 10.1093/bioinformatics/bts635.
58. Trapnell, C., Williams, B.A., Pertea, G., Mortazavi, A., Kwan, G., van Baren, M.J., Salzberg, S.L., Wold, B.J., and Pachter, L. (2010). Transcript assembly and quantification by RNA-Seq reveals unannotated transcripts and isoform switching during cell differentiation. Nat Biotechnol *28*, 511-515. 10.1038/nbt.1621.

59. Anders, S., Pyl, P.T., and Huber, W. (2015). HTSeq--a Python framework to work with high-throughput sequencing data. Bioinformatics *31*, 166-169. 10.1093/bioinformatics/btu638.

60. Love, M.I., Huber, W., and Anders, S. (2014). Moderated estimation of fold change and dispersion for RNA-seq data with DESeq2. Genome Biol *15*, 550. 10.1186/s13059-014-0550-8.

SUPPLEMENTARY MATERIALS

Figs. S1–S5

Tables S1 to S5

Figure S1. Sequencing confirmation of APOE3 and APOE3S/S knockin mice

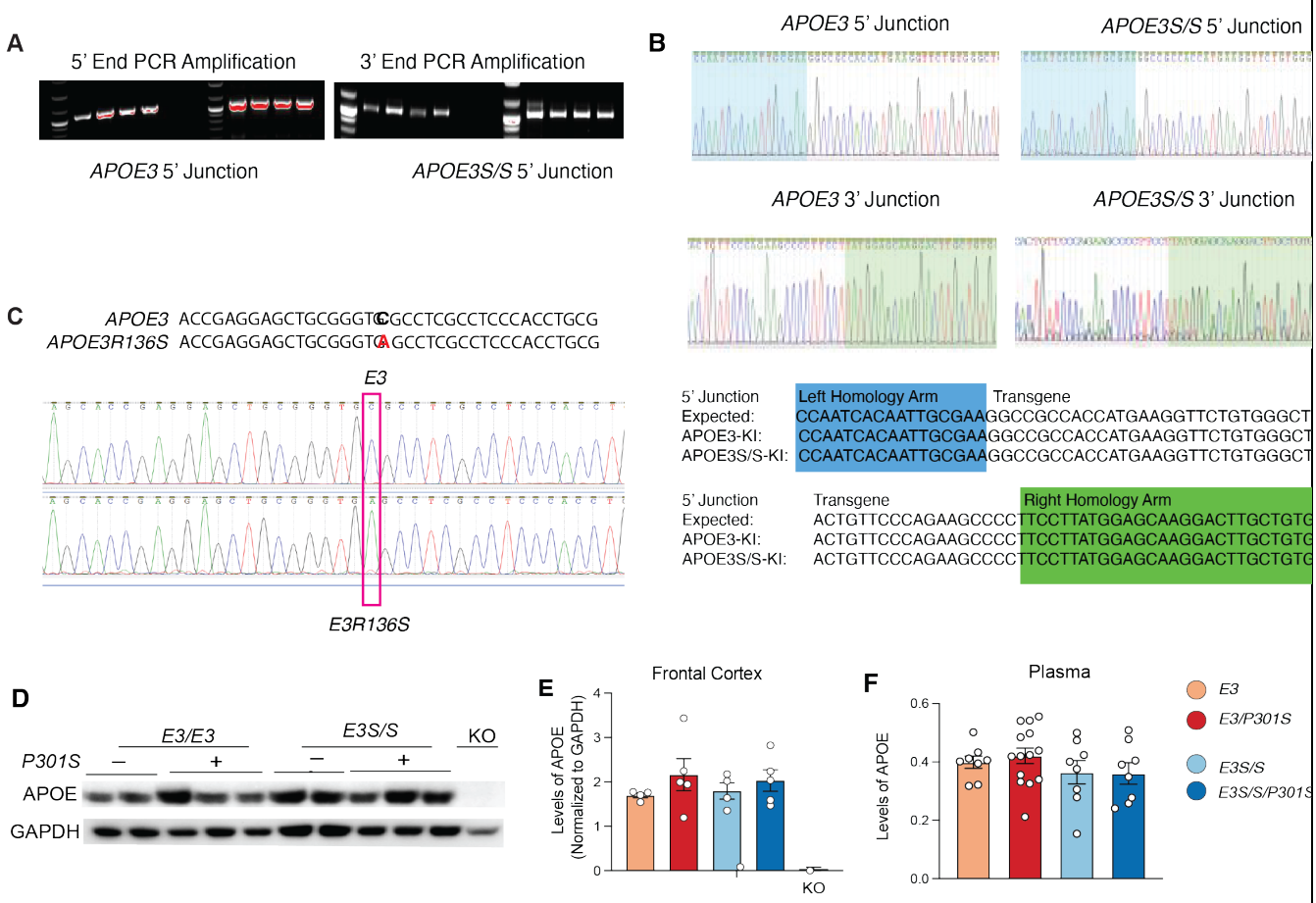

Figure S1. Sequencing to confirm the model and no APOE changes among any experimental groups. Related to **Figure 1**.
(A) Representative gel for PCR amplification to show insertion of the *E3*$^{S/S}$.
(B) Sequence of human APOE3-KI and human APOE3S/S-KI.
(C) Confirmation of *R136S* mutation using Sanger sequencing.
(D) Representative western blot of human APOE levels in frontal cortex lysates of male mice from each experimental group.
(E) Quantification of APOE levels normalized to GAPDH, showing no differences in experimental groups.
(F) Plasma levels of APOE collected from all four experimental groups at 9-10 months in male mice, also showing no significant differences between experimental groups.

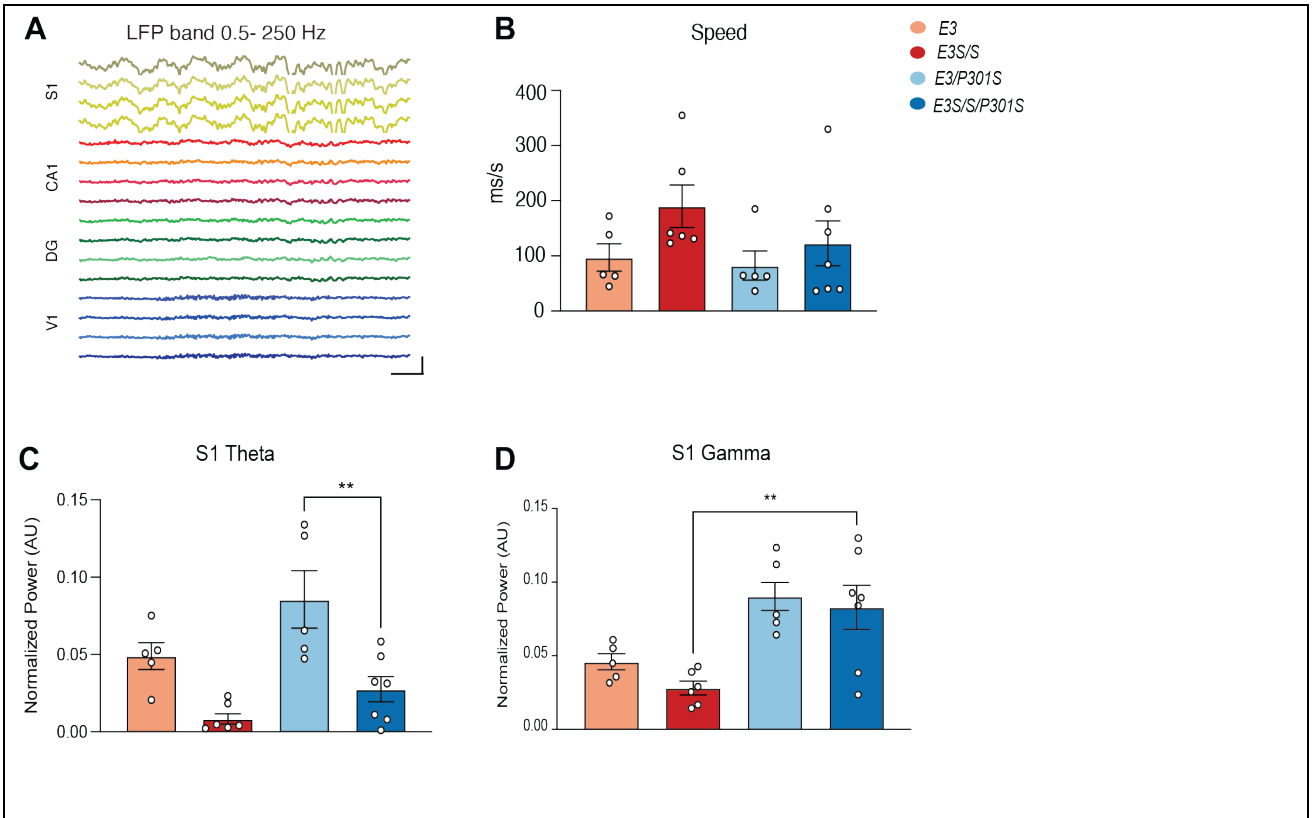

Figure S2. *R136S* affects tau-induced deficits in network dysfunction. Related to **Figure 1**.
(A) Example LFP trace showing recordings from S1, CA1, DG and V1 regions.
(B) Quantification of average speed during the open field exploration period showing no significant differences among groups. N= 5 for *E3*, n=6 for *E3/P301S, n*= 5 for $E3^{S/S}$, n= 7 $E3^{S/S}$*/P301S*. Data were analyzed by two-way ANOVA with mixed-effects model.
(C) Quantification of average S1 theta power across all four groups, showing tau-induced decreases in power in both *E3* groups. N= 5 for *E3*, n=6 for *E3/P301S, n*= 5 for $E3^{S/S}$, n= 7 $E3^{S/S}$*/P301S*. *p=0.0217 and p=0.022, respectively. Data were analyzed by two-way ANOVA with mixed-effects model.
(D) Quantification of average S1 gamma power across all four groups, showing lack of decrease in power in $E3^{S/S}$*/P301S* in comparison to *E3/P301S*. N= 5 for *E3*, n=6 for *E3/P301S, n*= 5 for $E3^{S/S}$, n= 7 $E3^{S/S}$*/P301S*. *p=0.0116. Data were analyzed by two-way ANOVA with mixed-effects model.

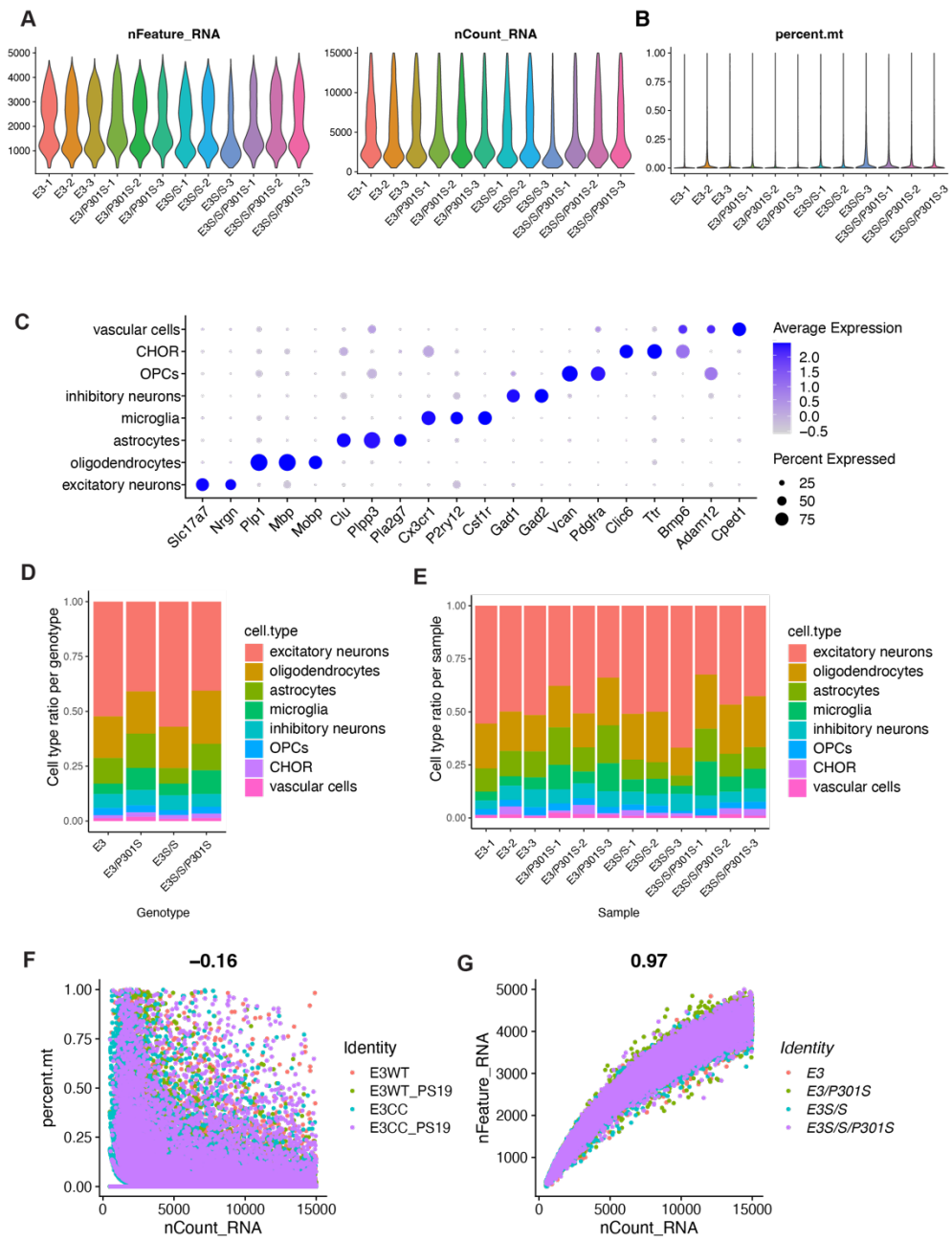

Figure S3. Quality control assessment of single nuclei RNA sequencing data of the *E3* and *E3*$^{S/S}$ tauopathy mice, related to **Figures 3, 4, 5.**

(A) Quality-control plots showing equivalent amounts of total RNA features, total number of RNA counts.

(B) Violin plot showing percentage of mitochondrial genes detected per nuclei for each individual sample.

(C) Dot plot showing expression of identity markers for each cell type.

(D) Proportion of each cell type within differing *E3* and *E3*$^{S/S}$ genotypes.

(E) Proportion of each cell type within individual samples.

(F and G) Correlation between UMI counts and percentage of mitochondrial genes detected (F) or total gene counts (G) per nuclei for each individual sample.

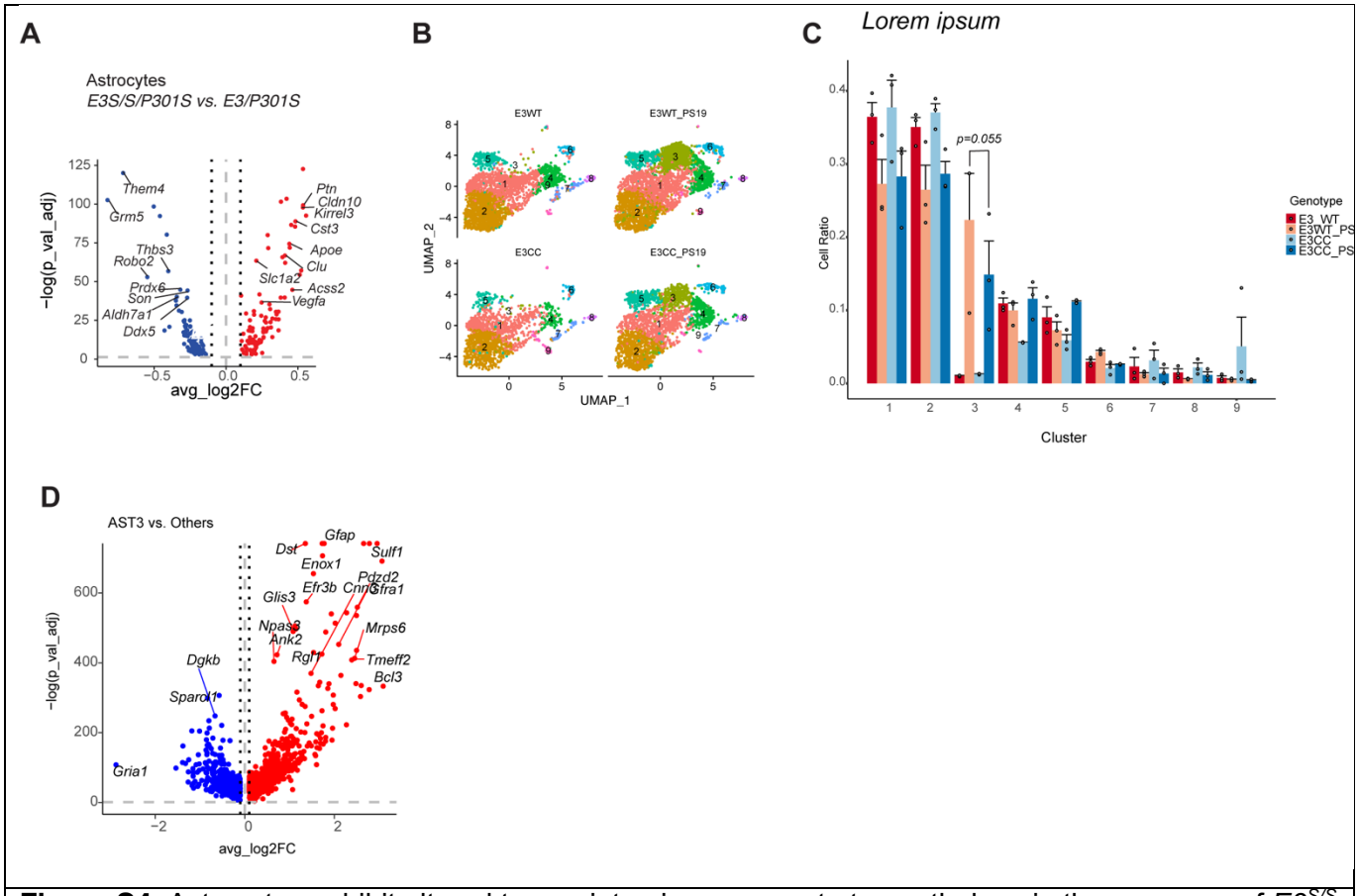

Figure S4. Astrocytes exhibit altered transcriptomic response to tau pathology in the presence of *E3$^{S/S}$*
Related to **Figures 3, 4, 5.**
(A) Volcano plot of DEGs in astrocytes between *E3$^{S/S}$/P301S* and *E3/P301S*. Dashed lines represent log2foldchange threshold of 0.1 and adjusted p value threshold of 0.05.
(B) UMAP of astrocyte subclusters split by genotype.
(C) Quantification of cell ratios within each subcluster.
(D) Volcano plot of DEGs in astrocyte subcluster 3 versus all other subclusters.

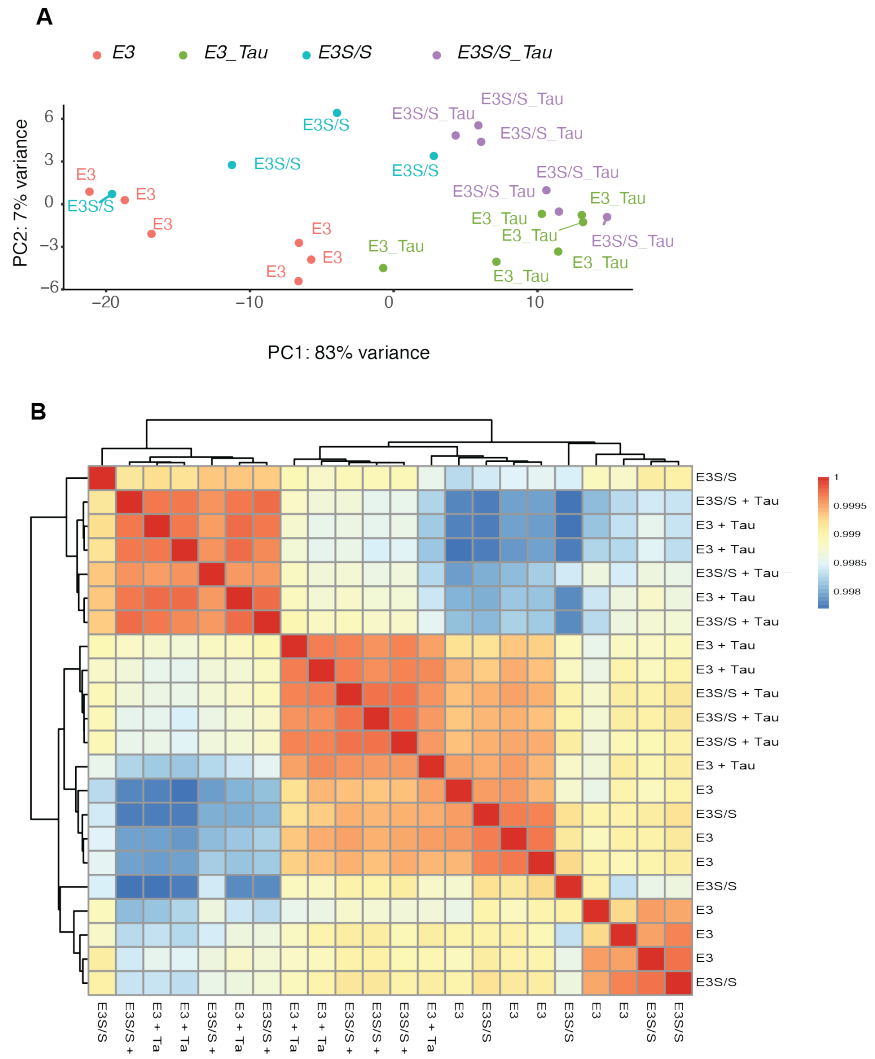

Figure S5. Quality control assessment of bulk RNA sequencing data of *E3* and *E3$^{S/S}$* primary microglia, related to **Figure 5**.
(A) Principal component analysis plot. Tau fibril stimulation accounts for 83% of gene expression variance. Each circle represents one biological sample.
(B) Heatmap showing correlations between each biological sample. Samples cluster based on *APOE3* genotype and tau stimulation status. There are no outlier samples.

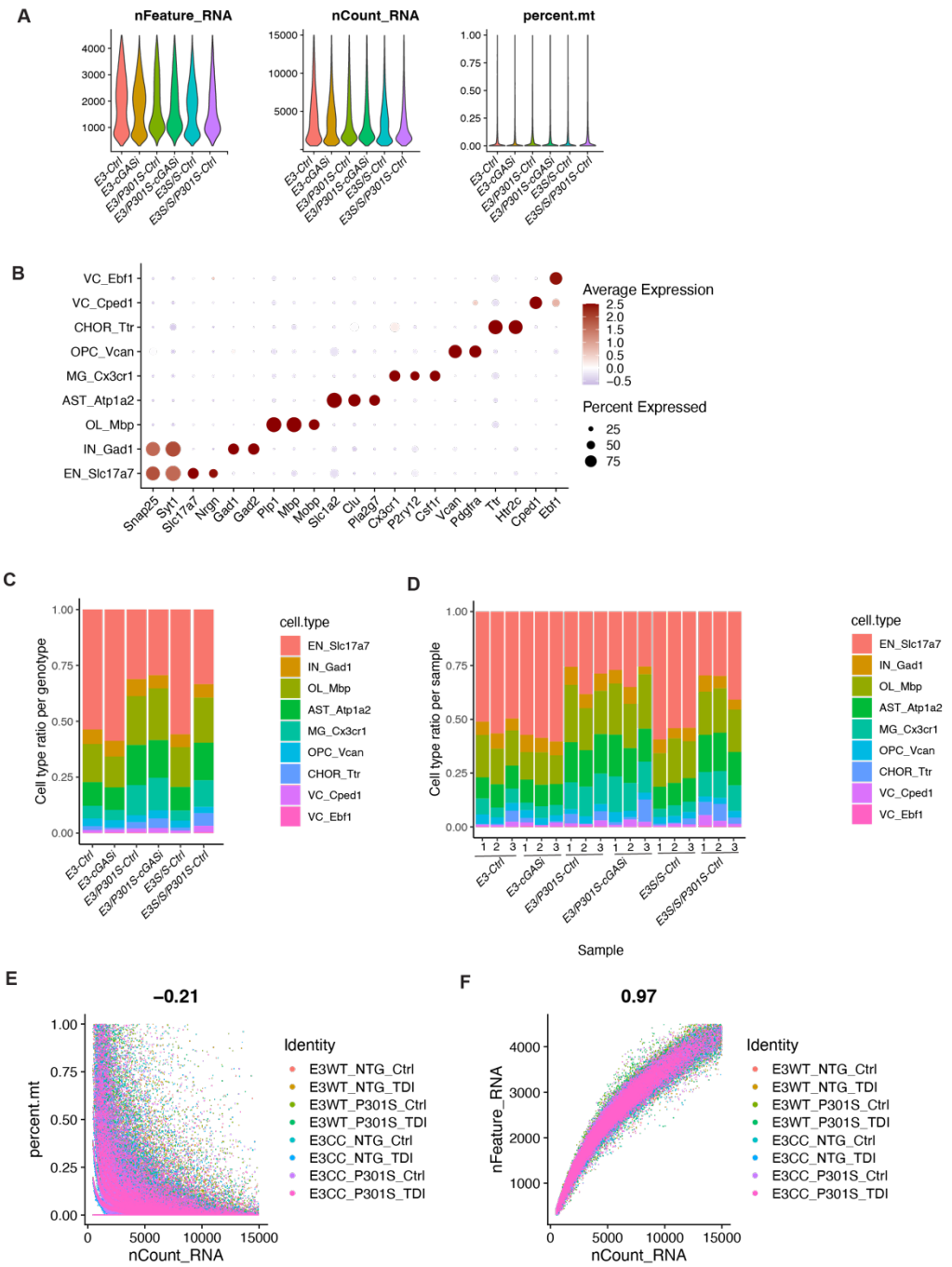

Figure S6. Quality control assessment of single nuclei RNA sequencing data of the *E3* and *E3*$^{S/S}$ tauopathy mice, related to **Figure 6**.
(A) Quality-control plots showing equivalent amounts of total RNA features, total number of RNA counts, showing percentage of mitochondrial genes detected per nuclei for each individual sample.
(B) Dot plot showing expression of identity markers for each cell type.
(C) Proportion of each cell type within differing *E3* and *E3*$^{S/S}$ genotypes, treated with either cGAS-inhibitor diet or control diet.
(D) Proportion of each cell type within individual samples.
(E–F) Correlation between UMI counts and percentage of mitochondrial genes detected (E) or total gene counts (F) per nuclei for each individual sample.